



A Comparison of Hybrid-Electric Aircraft Sizing Methods

D. Felix Finger*

*Department of Aerospace Engineering, FH Aachen University of Applied Sciences, Aachen, Germany
and*

School of Engineering, RMIT University, Melbourne, Australia

Reynard de Vries†, Roelof Vos‡

Faculty of Aerospace Engineering, Delft University of Technology, Delft, The Netherlands

Carsten Braun§

Department of Aerospace Engineering, FH Aachen University of Applied Sciences, Aachen, Germany

Cees Bil**

School of Engineering, RMIT University, Melbourne, Australia

The number of case studies focusing on hybrid-electric aircraft is steadily increasing, since these configurations are thought to lead to lower operating costs and environmental impact than traditional aircraft. However, due to the lack of reference data of actual hybrid-electric aircraft, in most cases, the design tools and results are difficult to validate. In this paper, two independently developed approaches for hybrid-electric conceptual aircraft design are compared. An existing 19-seat commuter aircraft is selected as the conventional baseline, and both design tools are used to size that aircraft. The aircraft is then re-sized under consideration of hybrid-electric propulsion technology. This is performed for parallel, serial, and fully-electric powertrain architectures. Finally, sensitivity studies are conducted to assess the validity of the basic assumptions and approaches regarding the design of hybrid-electric aircraft. Both methods are found to predict the maximum take-off mass (MTOM) of the reference aircraft with less than 4% error. The MTOM and payload-range energy efficiency of various (hybrid-) electric configurations are predicted with a maximum difference of approximately 2% and 5%, respectively. The results of this study confirm a correct formulation and implementation of the two design methods, and the data obtained can be used by researchers to benchmark and validate their design tools.

Nomenclature

A	= aspect ratio [-]	E^*	= specific energy [J/kg] or [Wh/kg]
C_D	= drag coefficient, $D/(0.5\rho_\infty V_\infty^2 S)$ [-]	e	= Oswald's aircraft efficiency factor [-]
$C_{D,\min}$	= minimum drag coefficient [-]	h	= altitude [m]
C_L	= lift coefficient, $L/(0.5\rho_\infty V_\infty^2 S)$ [-]	H_p	= hybridization ratio [-]
$C_{L,\max}$	= maximum lift coefficient [-]	k	= induced drag factor [-]
$C_{L,\min D}$	= minimum-drag lift coefficient [-]	L	= lift [N]
D	= drag [N]	L/D	= lift-to-drag ratio [-]
E	= energy [J]	m	= mass [kg]

* PhD Candidate, FH Aachen UAS / RMIT University, f.finger@fh-aachen.de, AIAA Student Member

† PhD Candidate, Delft University of Technology, r.devries@tudelft.nl, AIAA Student Member

‡ Assistant Professor, Delft University of Technology, r.vos@tudelft.nl, AIAA Associate Fellow

§ Professor, FH Aachen UAS, c.braun@fh-aachen.de, AIAA Member

** Professor, RMIT University, cees.bil@rmit.edu.au, AIAA Associate Fellow

M	=	Mach number [-]	div	=	diversion
p	=	pressure [Pa]	EM	=	electrical motor or machine
P	=	power [W]	f	=	fuel
P^*	=	specific power [kW/kg]	GB	=	gearbox
P/W	=	power-to-weight ratio [W/N]	GEN	=	electrical generator
R	=	Range [km]	GT	=	gas turbine
Re	=	Reynolds number [-]	HEP	=	hybrid-electric propulsion
S	=	wing reference area [m^2]	ISA	=	international standard atmosphere
T	=	thrust [N]	miss	=	nominal mission (excl. reserves)
V	=	velocity [m/s]	MGC	=	mean geometric chord
V_s	=	stall speed [m/s]	MSL	=	mean sea-level
W	=	weight [N]	MTOM	=	maximum take-off mass
W/P	=	power loading [N/W]	OEI	=	one engine inoperative
W/S	=	wing loading [N/m ²]	OEM	=	operating empty mass
α	=	angle of attack [deg]	OEM'	=	OEM without propulsion system mass
$\Delta(\dots)$	=	change in aerodynamic property	p	=	propulsive
ε	=	stopping criteria [-]	PH	=	parallel-hybrid
η	=	efficiency [-]	PL	=	payload
μ	=	dynamic viscosity [Pa·s]	PMAD	=	power management and distribution
ρ	=	density [kg/m ³]	PREE	=	payload-range energy efficiency
Φ	=	supplied power ratio [-]	ROC	=	rate-of-climb
<i>Acronyms / Subscripts</i>					
AEO	=	all engines operating	s	=	shaft
bat	=	battery	SH	=	serial-hybrid
BSFC	=	brake-specific fuel consumption	SL	=	sea-level
cr	=	cruise	TO	=	take-off
			VTOL	=	vertical take-off and landing
			∞	=	freestream conditions

I. Introduction

THE reduction of greenhouse gases is a relevant topic in every field of today's research. For land-, water-, and air-based traffic, electric propulsion is a potential solution to achieve a reduction in emissions and minimize the use of fossil fuel. Fully electric cars and ships are already in mass production (see e.g. Refs. [1,2]), but only a small number of experimental aircraft currently use electric propulsion technology. This is mainly due to the current battery technology, which limits flight endurance and range [3]. Until battery technology is mature enough [4], hybrid-electric powered aircraft could help further reduce emissions, fuel burn, and noise. Interest in hybrid-electric aircraft design has significantly increased, as shown by the growing number of publications on this topic [5]. However, design procedures and best practices for hybrid-electric aircraft are yet to be developed [6]. In this context, one of the main challenges is the initial sizing of hybrid-electric aircraft, that is, the process of going from the first concept to a baseline design with component masses and engine power that reflect the top-level aircraft requirements.

Many studies are conducted exploring the design space of this new technology. However, these studies often lack transparency regarding the aircraft sizing process. Furthermore, the results of hybrid-electric design studies are usually – if not always – presented without any validation or uncertainty quantification, despite the use of novel design methods. This can, at least partly, be attributed to the fact that validation and verification of design tools for hybrid-electric aircraft is a very challenging task due to the lack of available validation data. On the one hand, validation data from existing design studies are scarce because most research does not explicitly list assumptions nor provide sufficient quantitative data to replicate the designs. On the other hand, given that hybrid-electric propulsion is an emerging technology, there are only a very limited number of manned hybrid-electric aircraft that have been flight tested. Examples of hybrid-electric aircraft include a modified motor glider built by the University of Cambridge [7],

a retrofitted Cessna 337 by Ampaire¹, and a modified DA40 built by Diamond Aircraft². Since all these aircraft are experimental or prototypes with hybrid-electric propulsion systems fitted to existing conventional aircraft, they are not representative of a fully optimized clean-sheet design, and moreover, only a limited amount of data is publicly available.

At FH Aachen and TU Delft, sizing tools for hybrid-electric aircraft have been independently developed in parallel over the past years. In both approaches, the traditional preliminary sizing methods (Refs. [8-13]) were modified to account for hybrid-electric propulsion. The method developed at FH Aachen focuses on the design of general aviation aircraft with special focus on vertical take-off and landing (VTOL). The approach of TU Delft focuses on the design of transport aircraft with special focus on the aero-propulsive effects associated with distributed-propulsion or boundary-layer-ingestion configurations. Both methodologies are designed to provide a first analysis of the available design space for a set of top-level requirements and to determine power-to-weight ratio (P/W_{TO}), wing loading (W_{TO}/S) and hybridization of power (i.e., the split between electric power and combustion engine power).

In this paper, the two methodologies are compared with the aim of assessing if the general approach to the sizing of hybrid-electric aircraft is valid. The assumptions, discrepancies, and results provided by the two methods are discussed in order to maximize transparency and to provide data to the aircraft design community to benchmark and validate hybrid-electric design tools.



Fig. 1 Comparison between Do 228NG [14] (left) and the 19-seat baseline aircraft (right).

To establish a common baseline, a 19-seat commuter aircraft is used. This reference aircraft is based closely on the Dornier/RUAG Do 228NG, shown in Fig. 1. This aircraft has been analyzed in previous hybrid-electric aircraft studies (see e.g. Refs. [15,16]). Moreover, performance data of the aircraft is available from multiple sources [17-20], and therefore it is well-suited as a reference configuration. First, this baseline aircraft is sized for a common set of top-level requirements and a conventional turboprop propulsion system. This will show the level of accuracy of the traditional approaches of the sizing methods when comparing the results with data for the Do 228NG. Then, hybrid-electric propulsion technology is introduced. Both methods are used to resize the aircraft under consideration of serial, parallel, and fully-electric propulsion system architectures. In this context, resizing is the process of re-matching the aircraft's mass to its desired performance, with only the top-level requirements maintained constant. The results are compared, and differences are highlighted. Finally, in order to verify that the trends of the different approaches match, a sensitivity study is conducted. With this, the gradient of any figure of merit with regard to the analyzed parameters can then be determined, illustrating the impact of each parameter on the final design, and showcasing the differences between both methods. In this way, the study presented in this paper helps to build confidence in the design methods for hybrid-electric aircraft and to understand the impact that hybrid-electric propulsion systems have on the initial sizing process.

¹ N. Zazulia, "Hybrid-Electric Cessna 337 Takes Maiden Flight," Avionics International, 6 June 2019. Online. <http://www.aviationtoday.com/2019/06/06/ampaire-hybrid-electric-cessna-flight/>.

² A. M. Lentsch, "Diamond Aircraft 1st Flight Multi-engine Hybrid Electric Aircraft," 7 Nov 2018. Online. <http://www.diamond-air.at/en/media-center/press-releases/news/article/diamond-aircraft-1st-flight-multi-engine-hybrid-electric-aircraft/>.

II. Approach

In this section, the design methods of FH Aachen (Sec. II.A.1) and TU Delft (Sec. II.A.2) are briefly described. The main differences between the two methods are then summarized in Sec. II.B. Finally, Sec. II.C describes the simplified powertrain representations and parameterizations used by the two methods.

A. Sizing Methods

1. Method A: FH Aachen

The design methodology formulated at FH Aachen focuses on the design of general aviation aircraft with special focus on vertical take-off and landing (VTOL). The methodology of the sizing process is documented in Ref. [21]. Conventional take-off and landing general aviation aircraft were studied, as shown in Refs. [22-26]. The sizing of VTOL aircraft is discussed in Ref. [27]. The FH Aachen method is developed for aircraft with both parallel-hybrid and serial-hybrid propulsion systems, although it is applicable to conventional propulsors or fully electric propulsion systems as well. Therefore, the algorithm can be integrated into existing design or analysis tools. Its goal is the identification of the optimal design point (P/W_{TO} and W_{TO}/S) of such aircraft and, in addition to this, the corresponding degree of hybridization. Analogous to the classical methods, the methodology is separated into two major parts: point performance, also referred to as the constraint diagram, and mission performance, also known as the mass estimation. For both parts, certain input parameters are necessary, representing the Top-Level Aircraft Performance Requirements (TLARs), which are defined for the individual aircraft. These requirements specify the TLARs, including the flight mission, the aerodynamics, and the propulsion system (number of engines, conventional, serial- or parallel-hybrid, etc.) and its corresponding efficiencies.

An overview of the process is shown in Fig. 2. In the first step, the point performance tool determines the constraint diagram. The required P/W_{TO} , with respect to the W_{TO}/S , is determined for constraints like the desired rate of climb, the desired take-off distance, or the desired cruise airspeed. The mission performance analysis is based on a classical iterative process presented in most aircraft design books (see e.g. Refs. [8,9]). To cover the mix of consumable (fuel) and non-consumable (batteries) energy sources on board, the masses are not treated as fractions, as it is usually done in other sizing algorithms (see e.g. Ref. [10]), but as absolute values. Additionally, the classical endurance and range equations of Breguet are not used to determine mass or energy fractions. Instead, the mission is broken into a large number of short segments and simulated, using a universally valid, energy-based approach. The mission is defined explicitly by the requirements. The fuel mass and battery mass are determined by calculating the required energy for each time step of the flight phase. This energy is split into its consumable and non-consumable parts through the degree of hybridization of the corresponding flight phase and converted into the necessary thrust or power.

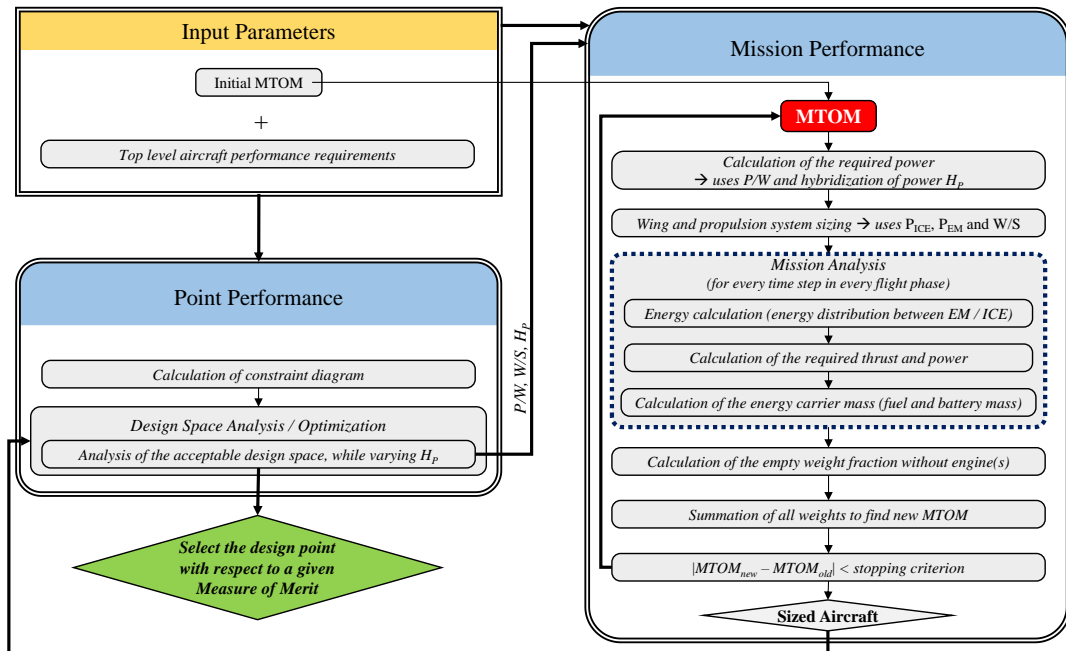


Fig. 2 Flowchart of the sizing process developed by FH Aachen [21].

Finally, based on a first estimate for the MTOM, all masses that make up the gross mass are calculated. This can be done by using Class-I or Class-II mass estimation methods. Using the results of the point performance analysis, the propulsion system is sized, as its engine, motor, and integration masses are estimated. In the final step, the empty mass is determined. Because the propulsion system mass is calculated separately, this mass fraction covers the usual operating empty mass without fuel, battery, and engine masses. Based on the new MTOM, the next iteration step can be started. The iteration stops when a certain mass convergence, defined by the stopping criteria ε , is reached.

2. Method B: TU Delft

The methodology developed at TU Delft focuses on the preliminary sizing of hybrid-electric transport aircraft, taking into account the aero-propulsive interaction effects present in novel propulsion-system layouts such as distributed propulsion, tip-mounted propulsion, or boundary-layer ingestion systems. The sizing process is documented in Ref. [28], and has been used in several configuration studies [29-31] and sensitivity studies [32,33] of hybrid-electric transport aircraft. Analogously to the approach of FH Aachen, the sizing method combines a point-performance analysis with a mission analysis and subsequent mass estimation, again using power-loading diagrams to represent the design space. However, the two methods differ in several aspects. The main advantages of the method developed by TU Delft are the inclusion of aero-propulsive interaction in the sizing process, and the use of a generic powertrain model which is independent of the type of architecture selected. The main disadvantages, on the other hand, are that the method is not applicable to VTOL and that it requires a more complex representation of the design space due to the use of multiple power-loading diagrams. This difference will be discussed in more detail in Sec. IV. An overview of the sizing method is presented in Fig. 3.

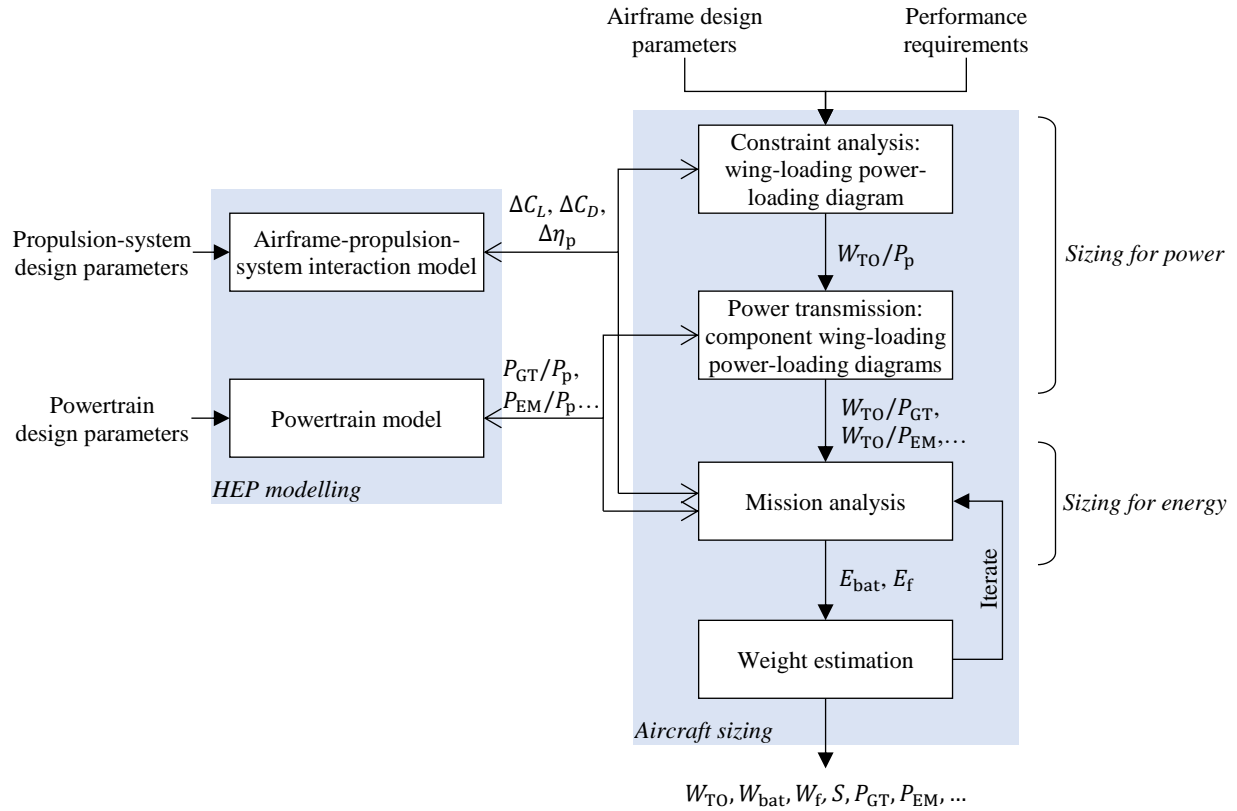


Fig. 3 Flowchart of the sizing process developed by TU Delft. Adapted from Ref. [34].

First, a constraint analysis is performed in order to determine the wing loading and power loading necessary in order to meet all top-level performance requirements. The point-performance equations used to determine the constraint curves are modified in order to include the changes lift, drag, and propulsive due to aerodynamic interaction between the propulsion system and the airframe. Once the performance constraints have been established in terms of

the required propulsive power ($P_p = T \cdot V$), a powertrain model is used to translate this requirement into a power requirement for each element in the powertrain, thus generating one power-loading diagram per component. This powertrain model is, essentially, a simplified matrix representation of the power balances across each element in the powertrain architecture. It requires up to three power-control variables (throttle, supplied power ratio, and shaft power ratio) to relate the propulsive power to the power required from the energy sources and the different components of the powertrain.

Once the powertrain components have been sized in terms of power using the power-loading diagrams, a mission analysis is performed to size the aircraft in terms of energy requirements. To this end, a time-stepping approach is performed over a simplified mission profile with an assumed initial MTOM, and the fuel energy and/or battery energy consumption is integrated along the mission. For this, the designer must specify the power-control strategy used during each mission segment. In other words, the throttle setting and power share between the different energy sources or propulsive devices must be specified as input, while the resulting degree-of-hybridization (of energy) is a result of the mission analysis. The resulting fuel and battery masses are included in a modified Class-I mass breakdown of the aircraft, and the MTOM is computed. With this updated MTOM, the mission analysis is re-evaluated until the aircraft mass converges.

B. Differences between Sizing Methods

Although both methods A and B stem from the well-known Class-I design methods, slightly different results must be expected due to differences in assumptions or modeling approaches. Different models are used for the constraint analysis, the mission analysis, and the systems analysis, with each model having individual strengths and weaknesses. In order to provide an overview, Table 1 highlights the key differences between methods A and B. For a more complete understanding of the rationale behind the two methods, the reader is referred to Refs. [28] and [35].

Both methods use the constraint diagram, also known as the “matching chart”, to derive the installed power. However, the main difference between the two methods is the use of a single, combined power-loading diagram in Method A, versus the use of multiple component-oriented power-loading diagrams in Method B. Consequently, Method A assumes a specific power split for all constraints, while Method B is more flexible but requires the designer to select a power split (i.e., a supplied power ratio; see Sec. II.C) for each constraint. The two approaches are described in detail when analyzing these diagrams for a hybrid-electric aircraft in Sec. IV.B. Moreover, a slightly different approach is used to determine the take-off and climb rate constraints. To determine the relationship between power, wing loading, and take-off distance, method A solves an analytic equation from Gudmundsson [10], which takes into account the aircraft’s drag and rolling friction. Method B uses a statistical approach based on $C_{L,TO}$, as described by Raymer [8]. To derive the climb rate constraints, the same approach is used to find excess power and thus climb rate; however, climb is performed at different speeds. Method A derives the speed for minimum drag power (maximum $C_L^{3/2}/C_D$), while method B assumes a stall margin of 1.2 V_s , since it is not possible to analytically derive the optimum climb speed when the aero-propulsive interaction effects are considered.

The same difference is reflected in the mission analysis, where Method A accelerates to the speed of minimum drag power, climbs, levels off at the desired altitude, and then accelerates to cruise speed. Method B, on the other hand, climbs at constant dM/dh , which leads to a smooth climb profile, but is less energy-efficient. A dM/dh profile is assumed for descent as well, at an idle throttle setting of 5%, for which the thrust produced is included in the point-performance equations. Method A handles descent more conservatively: a 10% throttle setting is considered as idle, but no residual thrust is considered during descent. In this case, the descent speed is adjusted to the velocity for best L/D . The taxi, take-off, and landing flight phases are also handled differently. Method A simulates the energy consumption of taxi phases by considering rolling friction, the taxi time and speed, and the take-off energy consumption by applying full power for a determined duration. The landing phase is considered part of the post-landing taxi. Method B covers these flight phases by using Roskam’s energy fractions [12], where statistical data is used to describe that part of the mission. In this study, the energy fractions assumed in Method B were selected to match the energy fractions computed in Method A. Furthermore, the fuel reserves required for loiter are computed in a different manner, as shown in Table 1.

Because method A was developed for reciprocating engines, as they are typically found for general aviation, the turboprop’s efficiency is described by BSFC values. Method B, on the other hand, describes the gas turbine’s thermal efficiency directly, using the factor η_{GT} . In both cases, the turboshaft efficiency is throttle (part-power) corrected, using an empirical formula for jet engines, as described in Ref. [8]. To prevent efficiency from reaching zero at 0% throttle, the BSFC values of method A have a certain maximum cut-off, whereas the efficiency is considered constant below 15% throttle by method B.

Finally, to model the operating empty mass (OEM), both methods use statistical Class I mass estimation methods for this comparison, even though Class II methods from Refs. [8,9,12] and [36] are implemented in Method A. However, Method A defines OEM' as the operating empty mass without a propulsion system. The propulsion system mass is added on top, to account for the large propulsion systems of VTOL aircraft, which are not covered by the typical statistical correlations. Method B considers a conventional OEM definition. For this comparative study, a constant empty-mass fraction is used. For the Do 228 data ($OEM/MTOM = 0.609$), statistics from Ref. [8] give an OEM/MTOM of approximately 0.6, with a decreasing trend with increasing MTOM. Statistics from Ref. [10] also give an OEM/MTOM of approximately 0.6, with an increasing trend with increasing MTOM. The sensitivity of the OEM fraction to MTOM was found to be small for the commuter class in both cases, and therefore a constant empty-mass fraction of $OEM/MTOM = 0.600$ was selected for Method B, and an equivalent mass fraction of $OEM'/MTOM = 0.545$ for Method A, which corresponds to the same value if the propulsion-system mass of the Do 228 is subtracted.

Table 1 Summary of the main differences between the two sizing methods.

Modeling approach	Method A	Method B
Loading diagram: Design-point selection	Single shaft-power diagram, relative size of components determined by power split	One diagram per component; size of each component determined in respective diagram
Loading diagram: Powertrain parametrization	Hybridization of installed power, H_p , applied simultaneously to all constraints in loading diagram	Supplied power ratio, Φ , specified for each constraint in loading diagram
Loading diagram: Take-off constraint	Gudmundsson's method, modified for offset drag polar (sensitive to drag and rolling friction)	Raymer's take-off-parameter
Loading diagram: Climb rate constraints	Performed at minimum drag power, $C_L^{3/2}/C_D$	Performed with a stall margin, $V = 1.2V_s$
Mission analysis: Taxi	Given taxi time and taxi speed, rolling friction must be overcome	Fuel/energy fractions
Mission analysis: Take-off / landing	Assume x minutes at a determined throttle setting	Fuel/energy fractions
Mission analysis: climb strategy	Climb at $C_L^{3/2}/C_D$ and then accelerate to cruise speed	Constant dM/dh ; leads to smooth profile but slightly higher energy consumption
Mission analysis: descent strategy	10% throttle (~idle), which consumes energy but produces no thrust; descent at best L/D speed	5% throttle (~idle), which produces some residual thrust
Mission analysis: Loiter	x minutes at constant altitude and flight speed, including transients to reach loiter speed and altitude	x minutes at constant altitude and optimum flight speed in terms of energy consumption; transients neglected
Turboprop/ Turboshaft efficiency	Constant above a given BSFC value	Constant below a given throttle setting
OEM/MTOM fraction	$OEM'/MTOM = 0.545$; OEM' excludes powertrain	$OEM/MTOM = 0.600$; OEM includes powertrain

C. Hybrid-electric powertrain definitions

Multiple different powertrain architectures can be conceived when considering (hybrid-) electric propulsion [37]. Different levels of modeling detail exist, depending on the focus of the design study. In the preliminary sizing methods treated in this paper, a simplified model is used where each component is treated as a “black box” with an associated weight and transmission efficiency. Although a more complete description of these simplified representations can be found in Refs. [38] and [28], a brief overview of the serial and parallel architectures is included here for clarity, to relate the different parameterizations of the two methods to each other.

The parallel hybrid architecture (Fig. 4a) is a configuration in which gas turbine (GT) and electric motor (EM) work in conjunction. Both are mechanically connected to a propeller shaft, often via a gearbox. The total required power is split between GT and EM by a certain degree of hybridization. This allows for a smaller combustion engine, as well as a small electric motor for a given total propulsive power P_p . Parallel hybrid architectures are typically a very efficient and light way to add electric power to an aircraft [38].

In a serial-hybrid system (Fig. 4b) the propulsor’s shaft is only driven by an EM, while the GT is used to generate electricity for the electric system. The electric system is supplemented by a battery. Sometimes, the unit of GT and generator (GEN) are referred to as a “range extender” (see e.g. Ref. [39]), depending on how the batteries and fuel-based engines are used throughout the mission. Depending on the layout of the system, the GT can run at a constant speed and power setting, which allows it to be optimized for one specific design point. Often, an additional power management system is employed, which can distribute energy between EM and battery, enabling in-flight re-charging of the battery. If the battery is sized accordingly, an aircraft with a serial-hybrid powertrain can also operate in an all-electric mode. This might be desirable from a noise or local emissions perspective.

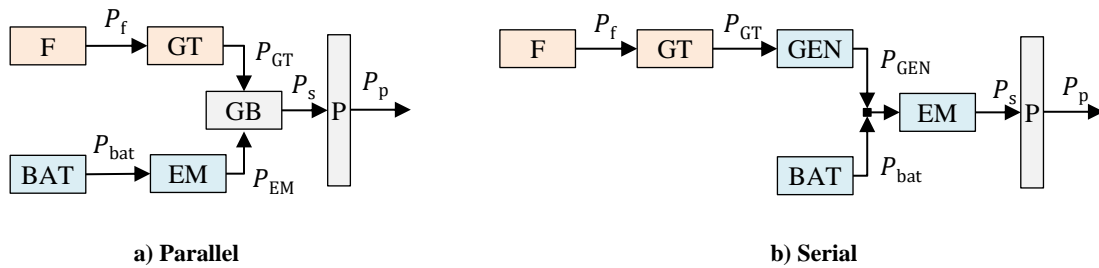


Fig. 4 Simplified representation of the parallel and serial powertrain architectures.

Parallel- and serial-hybrid propulsion systems should not be compared on a one-to-one basis, because this would not be a meaningful comparison. As shown in Refs. [22] and [35], a serial-hybrid system will typically perform worse than a parallel-hybrid system for a similar set of parameters. This is caused by the additional mass that the generator system will add to the aircraft, the corresponding reduction of powertrain efficiency, and the fact that the electric motor must be sized to deliver the total propulsive power. The advantage of serial-hybrid systems is their geometric flexibility. EMs can be installed independently of the location of the GT. This enables distributed propulsion layouts (see e.g. Refs. [32], [40], or [41]), which can take advantage of favorable aero-propulsion interaction. Thereby, the mass increase of the propulsion system is traded against improved aerodynamic efficiency. In this paper, aero-propulsive effects are not considered, to simplify the analysis and improve comparability. Consequently, all serial hybrid designs are expected to be outperformed by the parallel hybrid designs.

The two hybrid-electric propulsion systems shown in Fig. 4 have a mechanical and electrical node, respectively. Therefore, when compared to a conventional fuel-burning powertrain, additional degrees of freedom are available. Method A uses the parameter H_p to describe the hybridization. H_p is the level of hybridization of power, which for parallel architectures is the ratio of the propulsion power of EMs to the total propulsion power at the propeller shaft (see Eq. 1). Note that for serial hybrid-electric powertrains, $H_{p,ph}$, as defined in Eq. 1, is always equal to one since only the EM delivers the total installed power. To differentiate between the fully-electric powertrain and to size the generator, in this case, the parameter $H_{p,sh}$, is introduced by Eq. 2.

$$H_{p,ph} = \frac{P_{EM}}{P_{EM} + P_{GT}} \quad (1)$$

$$H_{P,SH} = \frac{P_{bat}}{P_{bat} + P_{GEN}} \quad (2)$$

This definition of $H_{P,SH}$ is different from the definition provided in Ref. [21]. Previous publications defined $H_{P,SH}$ as the ratio between P_{EM} and P_{GT} . This definition would result in a hybridization ratio of less than 1 for parallel hybrids, and larger than 1 for serial hybrids. For the sake of comparability, the definition is changed for this paper, so that the ratio H_P is less than 1 for both SH and PH, which makes it similar to the hybridization definition of method B.

Method B, on the other hand, uses the *supplied power ratio*, which can be expressed as

$$\Phi = \frac{P_{bat}}{P_{bat} + P_f} \quad (3)$$

Although this parameter governs the power split at the node (i.e., the gearbox for the parallel architecture, or the electrical node for the serial architecture), in this case, the supplied power ratio specifies the value of the split at the energy sources rather than at the node itself, unlike the parameter H_p . This formulation is necessary to apply the generalized matrix formulation used to solve the different powertrain architectures, as described in Ref. [28]. Since the definition of the two control variables differs only by the transmission efficiency of the components located between the energy sources and the nodes, they can easily be related to each other through:

$$\Phi = \begin{cases} \frac{1}{1 + \frac{\eta_{EM}}{\eta_{GT}} (1 - H_{P,PH})}, & \text{for parallel architectures} \\ \frac{1}{1 + \frac{1}{\eta_{GT}\eta_{GEN}} (1 - H_{P,SH})}, & \text{for serial architectures} \end{cases} \quad (4)$$

III. Baseline Reference Aircraft

To build confidence in the abilities of both methods, a conventional baseline reference aircraft is modeled first. For this study, a 19-seat, CS-23 commuter aircraft is selected. Commuter class aircraft (up to 8618 kg) are slightly larger than the general aviation category (up to 5760 kg), for which Method A is designed, and slightly smaller than the CS-25 transport aircraft, for which Method B is typically used. In this way, it is possible to verify that the approaches are generic enough for the sizing of hybrid-electric aircraft in general, and not just limited to the aircraft category for which they were initially intended. In this section, this baseline aircraft is sized for a given set of top-level requirements. This shows the level of accuracy of the traditional approaches of the sizing methods when comparing the results with data for the Do 228NG. These results are subsequently used as a baseline for the hybridization studies of Sec. IV.

A. Definition of Top-Level Aircraft Requirements and Design Assumptions

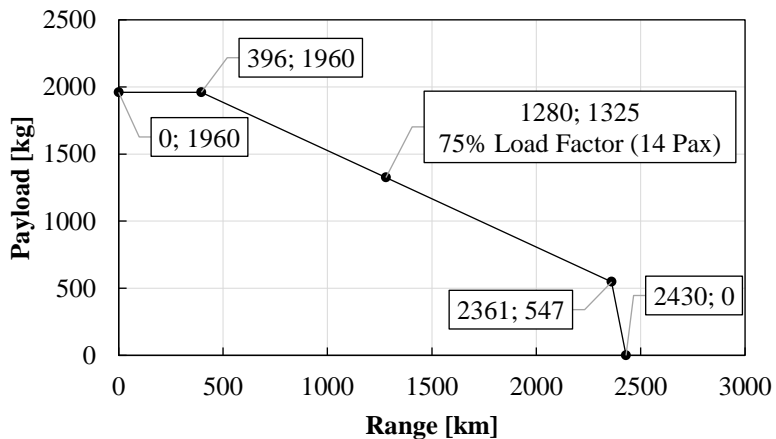
The reference aircraft is based closely on the Dornier/RUAG Do 228NG, a twin-turboprop STOL utility aircraft [42]. The Do 228 is built in conventional aluminum construction, features a high wing, and a rectangular-shaped fuselage. The fuselage is not pressurized. The landing gear retracts into a fuselage pod. For propulsion, Honeywell TPE331 engines are used. They are flat-rated to 579 kW when installed on the Do 228 [17], but are designed to produce up to 701 kW [19]. The reference aircraft is sized for a typical commuter mission, including diversion, 30 minutes of loiter, and additional contingency fuel reserves, as specified by the regulations [43]. The mission specification and top-level design requirements are shown in Table 2.

The selected aircraft performance requirements are based on information given in Refs. [17] and [20], while the propulsion system data is obtained from manufacturer data and the Do 228's pilot's operating handbook [18]. The following deviation was made from the published data. The published take-off distance is given as 793 m, including the climb to obstacle height. Using the pilot's operating handbook, take-off ground roll is determined as 650 m. Moreover, the mission requirements are extracted from the payload-range diagram of the aircraft, presented in Fig. 5.

Table 2 Mission and performance requirements.

Parameter	Value	Parameter	Value
Take-off distance [m]	793	Diversion speed V_{div} [m/s]	85
Taxi/Take-off altitude h_{TO} [m]	0	AEO ROC at SL [m/s]	8
Cruise altitude h_{cr} [m]	3000	OEI ROC at SL [m/s]	2
Landing/Taxi altitude h_{L} [m]	0	Range (baseline) R [km]	396
Diversion altitude h_{div} [m]	1000	Diversion range R_{div} [km]	270
Loiter altitude h_{loiter} [m]	450	Loiter time [min]	30
Cruise speed V_{cr} [m/s]	115	Contingency fuel [%]	5
Stall speed V_s [m/s]	34.5	Payload (baseline) m_{PL} [kg]	1960

The values of the design parameters and additional input assumptions selected to meet these top-level requirements are included in the Appendix for traceability. The aerodynamic modeling is discussed in Sec. III.B. The designs were found to be especially sensitive to the aerodynamic modeling of the aircraft and to the performance characteristics of the turboshaft engine. For the power lapse and specific fuel consumption (or thermal efficiency) of the engine, a surrogate model is built based on TPE331 performance data [19]. Due to the flat-rating of the TPE331 used on the Do228, the engine was found to be able to produce maximum power at all combinations of flight speed and altitude considered in this study. The specific fuel consumption of the engine, meanwhile, is computed as a function of flight speed and altitude using the surrogate model, and additionally corrected for part-throttle, as mentioned in Sec. II.B.

**Fig. 5** Payload-range diagram of the Do 228NG. Data taken from Ref. [17].

B. Aerodynamic Modelling

Because no aerodynamic data for the Do 228NG is available in the public domain, the aerodynamic performance had to be estimated by the authors. To increase fidelity, the authors decided against a classical drag buildup to determine the drag polar. The Do 228 features under-the-wing engines, which contribute considerably to interference drag and also reduce the wing efficiency [44]. Additionally, it has a box-shaped fuselage with multiple kinks and significant upsweep (see Fig. 1), which complicates drag estimation. Götten et al. [45] highlight that drag build-up models can give significantly wrong results when applied to non-standard aircraft configurations. Therefore, Reynolds Averaged Navier Stokes (RANS) CFD simulations were carried out to determine the drag polar of the concept. The reference geometry was created in OpenVSP using 3-view drawings of the Do 228NG.

The simulation was set up according to the recommendations outlined in Ref. [46]. The OpenVSP geometry was transferred to Siemens' simulation package StarCCM+ via the .STL standard. Then, the flow field about the models was simulated using a steady-state RANS approach, using the SST $k-\omega$ (Menter) turbulence model. Further details on this methodology can be found in Ref. [47]. The RANS equations were solved using the assumptions of incompressible

flow with a Semi Implicit Method for Pressure Linked Equations (SIMPLE) approach. The bullet-shaped flow field was divided into finite volumes using StarCCM+’s unstructured Cartesian cut cell mesher with a dedicated prism mesh, which discretizes the boundary layer. Boundary layer thickness was determined using the Schlichting’s methods [48], ensuring y^+ values below 1 on the aircraft’s surfaces. The surface mesh size was adjusted to give approximately 70 cells over the wing in chordwise direction. Lift and drag forces on the models’ bodies were obtained by integrating the cells’ shear stress tensor and their pressures. To decrease the computational effort, a half-model was used, and a symmetry condition was applied. Grid-independent results were then obtained for a mesh size of 18.4 million cells. StarCCM+’s mesh optimization scheme was employed, which improves cell skewness angles, cell aspect ratio, and volume change between cells. Further information on the simulation parameters is presented in Table 3. A sample pressure coefficient distribution is shown in Fig. 6.

Table 3 Operating conditions selected for the CFD simulations of the reference aircraft geometry.

Parameter	Value
Free stream velocity V_∞ [m/s]	55
Reference pressure p_∞ [Pa]	101,325
Density ρ_∞ [kg/m ³]	1.225
Dynamic viscosity μ [Pa·s]	$1.812 \cdot 10^{-5}$
Reynold’s number Re_{MGC} [-]	$6.967 \cdot 10^6$
Mach number M_∞ [-]	0.161
Turbulence intensity (inlet) [-]	1%
Turbulent viscosity ratio (inlet) [-]	10

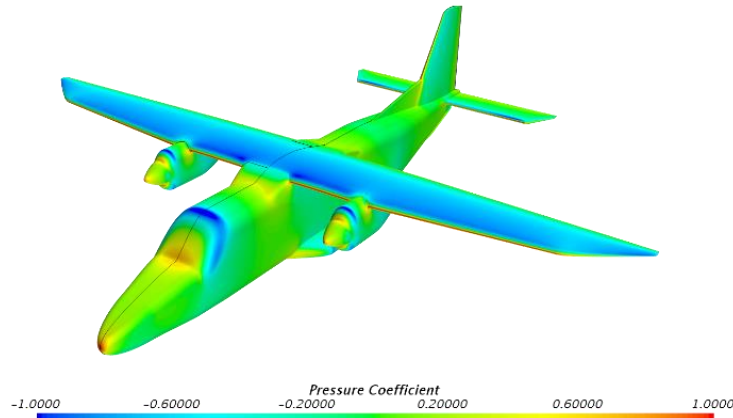


Fig. 6 Pressure coefficient distribution on the aircraft model at $\alpha = 0^\circ$. Propeller effects not included.

Nine operating points were calculated using this approach: from -4° to 10° angle of attack, in steps of 2° . Then a curve fit was applied to find the lift coefficient at minimum drag $C_{L,\min D}$, the minimum drag coefficient $C_{D,\min}$, and Oswald’s aircraft efficiency factor e . These parameters allow the construction of an asymmetric parabolic drag polar given by:

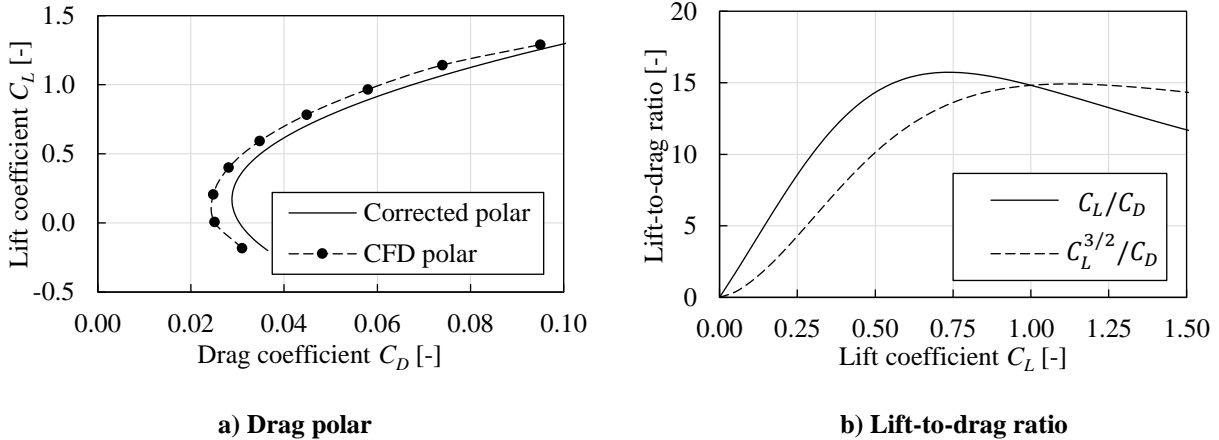
$$C_D = C_{D,\min} + k \cdot (C_L - C_{L,\min D})^2 \quad (5)$$

$$k = \frac{1}{\pi \cdot A \cdot e} \quad (6)$$

Additionally, a penalty was applied to the drag values obtained from RANS CFD since the drag from leakage and protuberance, cooling, propeller interaction, and other miscellaneous drag sources are not accounted for. A 20% increase of the total zero-lift drag is appropriate to account for the under-prediction of these effects by CFD [49]. The curve fit parameters are shown in Table 4. The simulation results are presented in Fig. 7. A maximum L/D of 16 is obtained at a C_L of 0.75.

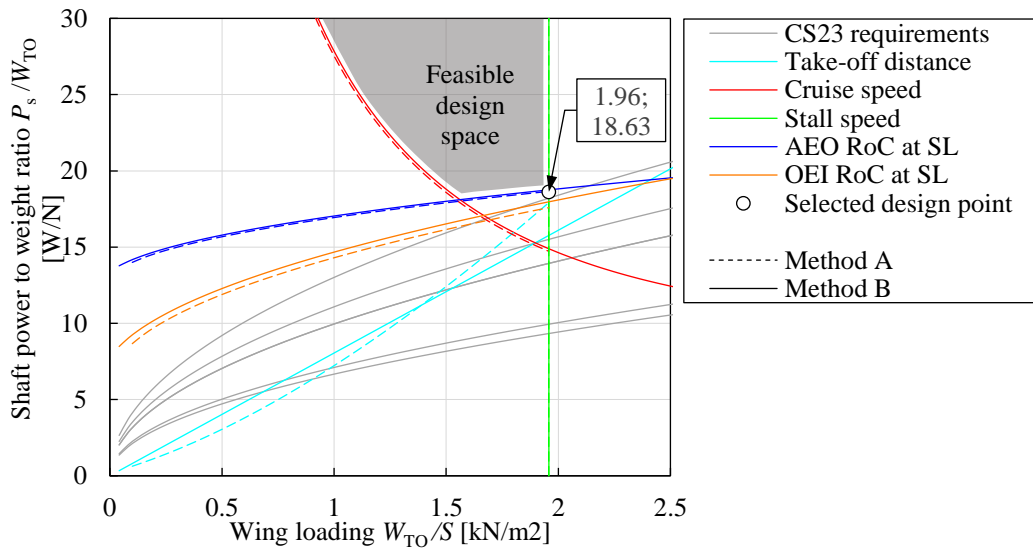
Table 4 Drag polar characteristics.

Parameter	Value
Aspect ratio A [-]	9.00
Minimum drag coefficient $C_{D,\min}$ [-]	0.029
Minimum-drag lift coefficient $C_{L,\min D}$ [-]	0.17
Oswald's aircraft efficiency factor e [-]	0.63

**Fig. 7** Drag polar characteristics obtained from the CFD simulations of the reference aircraft geometry.

C. Sizing of the Reference Aircraft

The first step of the sizing process is to determine the wing loading and power-loading or power-to-weight ratio of the aircraft. To this end, the results obtained from both methods for the Do 228 is shown in Fig. 8. The constraint lines are constructed with the requirements from Sec. III.A and the aerodynamic data from Sec. III.B. For completeness, all additional performance requirements specified by the regulations (Refs. [50,51]) have been included in grey lines in Fig. 8. However, these additional constraints were found to not actively constrain the design space, and are therefore not discussed in further detail.

**Fig. 8** Performance constraint diagram of the reference aircraft configuration, corrected to maximum throttle.

The agreement of both methods is good, although slight variations can be observed in the diagram. The most glaring disparity is the take-off distance constraint. Method A uses Gudmundsson's approach, which correlates W_{TO}/S and P_s/W_{TO} in a nonlinear fashion. Method B uses Raymer's linear regression approach, which gives more optimistic values at high wing loading. The one-engine inoperative (OEI) rate-of-climb (ROC) constraint at sea level (SL) is found to differ slightly due to the different flight speed assumed in either method (see Table 1), with method B being slightly more conservative. The all-engines operating (AEO) ROC constraint and the stall speed constraint, which determine the design point, are found to show a good agreement between the two methods, as well as the cruise speed constraint. Consequently, the design points obtained from both methods are practically identical, and differ less than 1% from the design point of the Do 228 for the selected design parameters, as shown in Table 5.

Table 5 Design point comparison.

Design Point	Do 228		Method A		Method B	
	Reference data	Value	Difference	Value	Difference	
W_{TO}/S [N/m ²]	1962	1957	-0.3%	1958	-0.2%	
P_s/W_{TO} [W/N]	18.44	18.65	+1.1%	18.63	+1.0%	

Using the P/W_{TO} and W_{TO}/S data from the constraint diagrams, the mission performance analysis is then carried out, and the energy requirements to match the desired mission. This is conducted for three different points of the Do 228's payload-range diagram: a short-range mission with maximum payload, a medium-range mission with 75% load factor, and a long-range mission that corresponds to maximum fuel and minimum payload (see Fig. 5). As the Do 228 flies all missions with the same MTOM, the sizing methods should also return the same gross mass for each of the points.

The sizing results of all points of the payload-range diagram are shown in Table 6 for both methods. The difference in MTOM between the reference aircraft and the sizing results of the numerical methods is less than 4%. This is a remarkable result, especially when considering that these methods are intended for conceptual design work, and the fidelity of the modeling is relatively low. As a general trend, Method A seems to be slightly too conservative when estimating MTOM (+0.5 to +3.8%), but no clear trend regarding the influence of the design range can be seen. Method B gets an excellent result (+0.3%) for the short mission, but slightly under-predicts MTOM for longer ranges (up to -3.3%). Furthermore, to verify that the MTOM estimation of the aircraft is correct and not an artifact of counteracting effects in the component mass estimation, the component masses of both methods for each mission are compared to reference data in Fig. 9. This figure shows that, apart from the fuel mass, both methods are capable of sizing the different components with reasonable accuracy.

Table 6 MTOM computed for the conventional aircraft configuration and comparison to reference aircraft data.

Mission	Range [km]	Payload [t]	Reference	Method A		Method B	
				MTOM [t]	MTOM [t]	Diff. [%]	MTOM [t]
	396	1.96	6.40	6.64	+3.8%	6.42	+0.3%
	1280	1.33	6.40	6.43	+0.5%	6.40	0.0%
	2361	0.55	6.40	6.49	+1.4%	6.19	-3.3%

Figure 9 shows that the largest discrepancy between the reference and the results of both methods is found for the fuel mass. Fuel mass is directly connected to the overall efficiency of the aircraft, and almost all modeling errors manifest themselves in an increase in fuel burn. The sensitivity of fuel burn to the aerodynamic characteristics of the aircraft and to the performance map of the turboshaft engine make the discrepancy hard to trace back to a specific assumption or modeling error. The largest relative difference is found for the short-range mission, which also has the lowest absolute fuel mass. Consequently, the relative deviation from the reference data is the largest, even though the fuel mass is only over-predicted by approximately 60 kg (see Table A.3). The larger error for shorter missions also suggests that different reserve-fuel requirements might play a role. For example, the diversion range of the reference aircraft might be lower than assumed here.

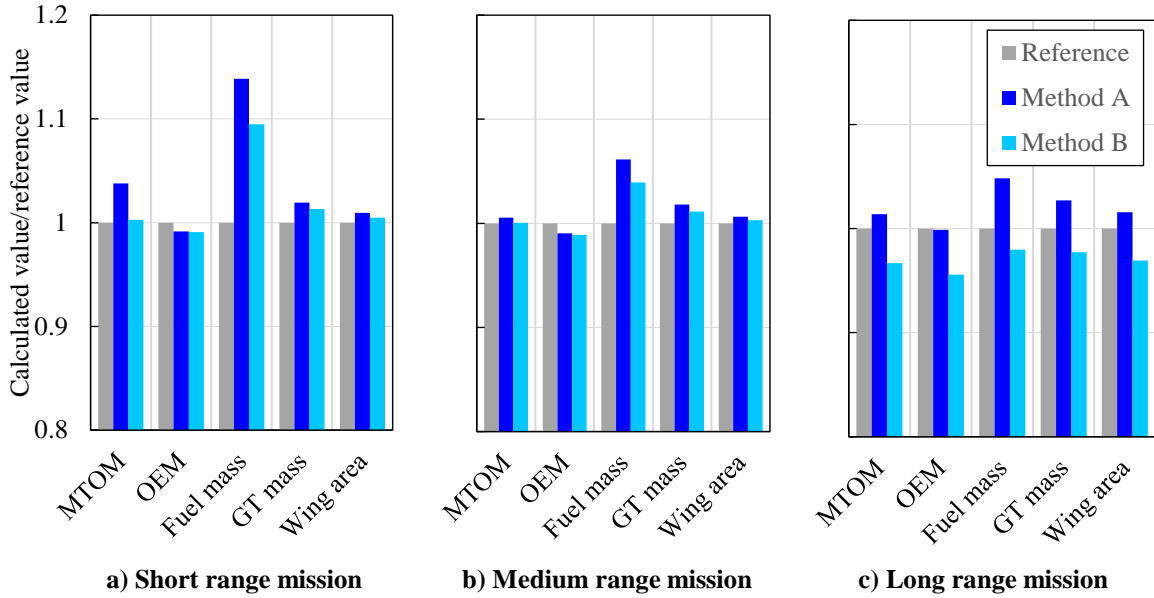


Fig. 9 Comparison between results obtained from the two sizing methods and reference aircraft data.

The inherent differences of the mission analyses of both methods play a factor as well: the taxi, take-off, and landing fuel fractions are calculated differently, a different climb and descent strategy is used, and the variable turboshaft efficiency is implemented differently, as discussed in Sec. II.B. Especially the last two points have an important effect for the shorter missions, as a larger fraction of the mission is spent in off-design conditions, instead of in cruise flight. To further investigate possible differences in the mission analysis, Fig. 10 shows the mission profile obtained by the two sizing methods for the short-range mission. Note that, for such a short mission, the reserves play an important role in determining the total fuel weight. Although no mission data is available for the reference aircraft, Fig. 10 shows that the two methods produce similar mission profiles. The climb and descent profiles of Method B are smoother but lead to slightly higher energy consumption, as discussed in Sec. II.B. Moreover, Method A explicitly models the taxi-out, take-off, landing, and taxi-in phases, while Method B does not. For Method B, the nominal mission starts at take-off speed and ends at the approach speed. Finally, Method A always accelerates/decelerates and climbs/descends between mission phases, while Method B presents a discontinuity at the beginning and end of the loiter phase, for which no transition phases are modeled. However, despite these differences, the block fuel consumption computed by the two methods does not differ significantly, as reflected in Fig. 9.

IV. Hybrid-Electric Aircraft

In this section, the conventional, parallel-hybrid, serial-hybrid, and fully electric aircraft are compared against each other. The comparison is conducted in detail for the three missions that were analyzed in Sec. III, and then, in more general terms, for three parameter sweeps.

A. Assumptions

The differences observed with the conventional baseline aircraft in Sec. III can largely be attributed to different modeling approaches for the mission reserves and powertrain components. To exclude these differences – which are not inherent to the formulation of the two sizing methods – several additional simplifications are made for the comparison of hybrid-electric aircraft. In this way, the additional discrepancies due to the incorporation of hybrid-electric propulsion can be isolated. In the following paragraphs, the simplifications are briefly explained.

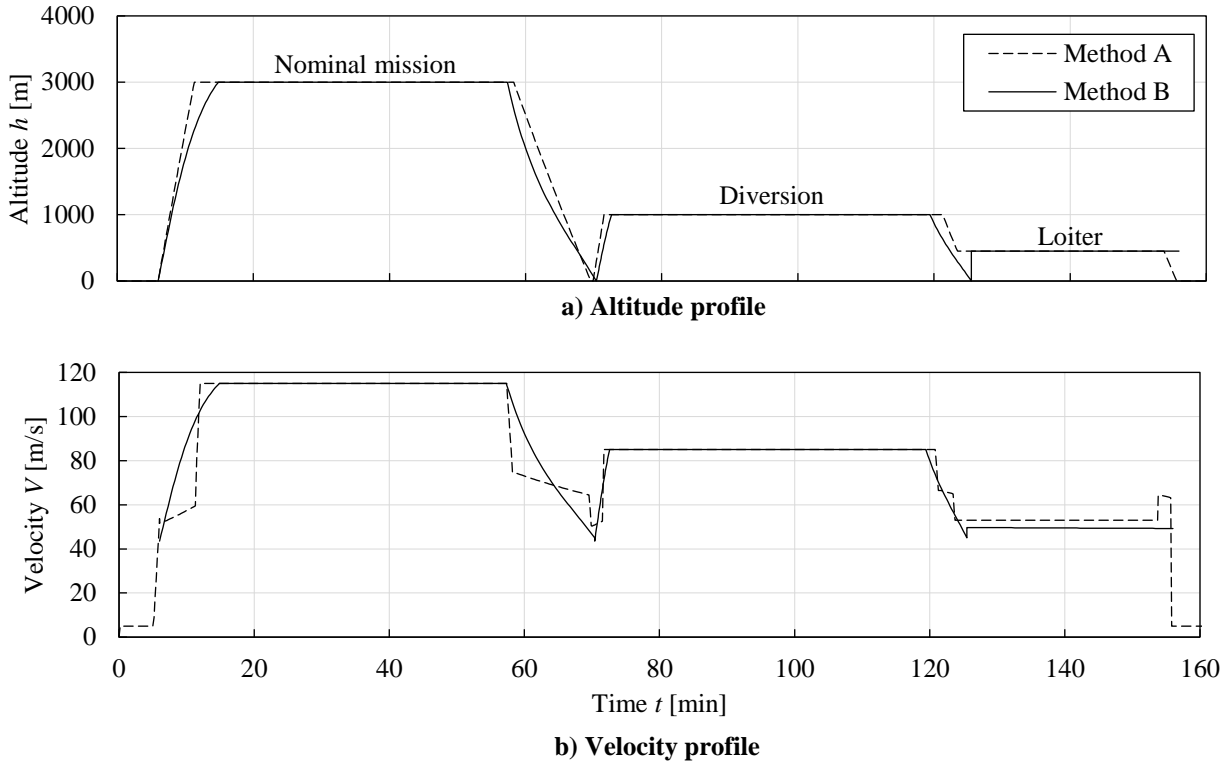


Fig. 10 Reference aircraft altitude (top) and velocity (bottom) profiles for the short-range mission.

1. Turboprop Engines

For the comparison of (hybrid-) electric concepts, the thermal efficiency of the gas turbines is fixed, independently of the throttle setting or flight condition, and assumed to be $\eta_{GT} = 0.2112$. This corresponds to a BSFC of 398 g/kWh, and is applied to both the (hybrid-) electric concepts and the conventional fuel-based reference aircraft, which is re-evaluated for this comparison. This value is obtained by calculating the average efficiency of the short-range mission, including the ground and diversion phases of the mission. Finally, the mass of the gas turbines is estimated using the specific power $P_{GT}^* = 3.31 \text{ kW/kg}$ of the Do 228's flat-rated TPE331 turboprop engines.

2. Electric Motors

The values of specific power and transmission efficiency assumed for the electrical machines (EM) and inverters/rectifiers are based on the state-of-the-art research goals presented in Ref. [52] and are gathered in Table 7. The EMs are assumed to achieve 13 kW/kg, and the specific power of the power converters is assumed to be 19 kW/kg. Since a thermal management system and additional elements of the power management and distribution (PMAD) system can significantly increase this system's mass, the total mass of the electrical systems is increased by 30%. This generic mass penalty is assumed due to a lack of information in the preliminary sizing phase for an accurate estimation of the mass of components such as cooling systems or cables. Thus, the equivalent specific EM mass is assumed to be 5.92 kW/kg. To describe the losses of the entire electrical system, a constant equivalent motor efficiency of 95% is used, and all other component's efficiencies are set to 100%.

3. Battery System

The battery system is modeled using a rudimentary “energy in a box” approach. Thus, an idealized constant potential battery is assumed. The internal resistance and other losses are assumed to be zero, and consequently, the efficiency of the battery is 100% (see Table 7). To preserve battery life and to account for energy reserves, a 20% state-of-charge margin is used. For the sake of comparison, futuristic technology assumptions are used, to allow for convergence of aircraft with high levels of hybridization and fully electric aircraft. With a specific energy $E_{bat}^* = 1500 \text{ Wh/kg}$ and a 4C discharge rate, reasonable MTOM values could be achieved. The selection of more realistic, near term battery technology would have resulted in too many unconverged design points. As the absolute results are of minor interest

for this comparative study, the authors preferred to select E_{bat}^* values, which allow for extensive parameter sweeps and comparisons. However, it is important to note that the technology values assumed for the batteries at pack level ($E_{\text{bat}}^* = 1500 \text{ Wh/kg}$ and $P_{\text{bat}}^* = 6 \text{ kW/kg}$) must be considered beyond optimistic. The maximum theoretical specific energy of Li-Ion batteries at cell level is 700 Wh/kg. Lithium-sulfur or aluminum-air batteries could reach such high specific energy levels in theory but are far from being usable in practical, high-power applications.

4. Mission Modelling

For conventional 19-seater aircraft, a 5% contingency fuel reserve has to be maintained [43]. Given that for HEP aircraft it is unclear whether these energy reserves should be accounted for in the fuel energy, battery energy, or both, this 5% contribution to total energy is not included in the following analyses. Thus, the fuel mass is reduced compared to the conventional short-range results.

Table 7 Characteristics assumed for powertrain components.

Parameter	Value	Parameter	Value
Turboshaft specific power $P_{\text{GT}}^* [\text{kW/kg}]$	3.31	Battery specific energy $E_{\text{bat}}^* [\text{Wh/kg}]$	1500
Turboshaft efficiency $\eta_{\text{GT}} [-]$	21.1%	Battery specific power $P_{\text{bat}}^* [\text{kW/kg}]$	6.0 (= 4C)
Electrical machine specific power (equivalent) $P_{\text{EM}}^*, P_{\text{GEN}}^* [\text{kW/kg}]$	5.92	Battery efficiency $\eta_{\text{bat}} [-]$	100 %
Electric machine efficiency (equivalent) $\eta_{\text{EM}}, \eta_{\text{GEN}} [-]$	95 %	Minimum state-of-charge [-]	20%

B. Comparison of Baseline Missions

In this section, the HEP variants are sized for the three reference missions presented in Sec III.A. Both methods differ in their approach to constructing the matching diagram, which is the first step of the sizing process. This is not only true with regards to the determination of the constraint lines, as discussed in Sec. III, but also with respect to the determination of the power split of the components of the hybrid-electric powertrain. To illustrate the difference, Fig. 11 presents a series of matching diagrams obtained from Method A and Method B. For both methods, only the five driving constraints (as discussed in Sec. III) are presented; other constraints from the certification specifications are neglected. As this example is only meant to further illustrate the different approaches of the methods, the matching diagrams are only shown for the parallel-hybrid propulsion architecture.

Method A attempts to simplify the matching process as much as possible. This allows using a graphical method to assess the hybrid electric design space. The results for any required figure of merit (e.g. MTOM, energy usage, or cost) can then be plotted and superimposed to the performance constraints. Such figures are sometimes called “thumbprint plots” and can be used to understand the hybrid-electric design space and select the best design point. More information can be found in Ref. [21]. However, finding a “best” design point is not the objective of this comparative study. Therefore, only a basic approach is explained: the constraint diagram is constructed, corrected to maximum throttle at sea level, as well as maximum take-off mass, and subsequently, the design point is selected. In Fig. 11, the design point is 18.63 W/N at a wing loading of 1.96 kN/m². To find the power required for a predetermined hybridization ratio, the total power-to-weight ratio, P/W_{TO} , is split by the hybridization ratio. For the example in Fig. 11, a P/W_{TO} of 16.76 W/N is selected for the gas turbine, while the remaining difference between gas turbine power and total installed power is provided by the electric power system. In other words, a hybridization of 10% is used, and thus $P_{\text{GT}}/W_{\text{TO}} = 16.76$, and $P_{\text{EM}}/W_{\text{TO}} = 1.87$. Because the normalization to maximum throttle at sea level is carried out before the power is split, the electric powertrain components are slightly oversized.

Method B, on the other hand, allows the designer to specify different power-control parameters (i.e., throttle and supplied power ratio) for each performance constraint. Hence, different components can be sized by different constraints, and none of the components is over-sized. For example, if the batteries and electromotor were only used during climb, then they would be actively sized in that condition, while the gas-turbine would have to provide only part-power, and would, therefore, be sized by a different constraint such as take-off or cruise. However, compared to Method A, this requires the designer to specify additional control settings, leading to a more complex interpretation of the matching diagrams, as evidenced in the bottom half of Fig. 11. This figure shows how first the shaft-power matching diagram is constructed (Fig. 11.B.1), based on which the matching diagrams of the remaining elements of the powertrain (see Fig. 4) are computed for a given power split. Since the power split is kept constant for all performance constraints in this study ($H_p = 0.1$), the relative positions of the constraints do not change much, although

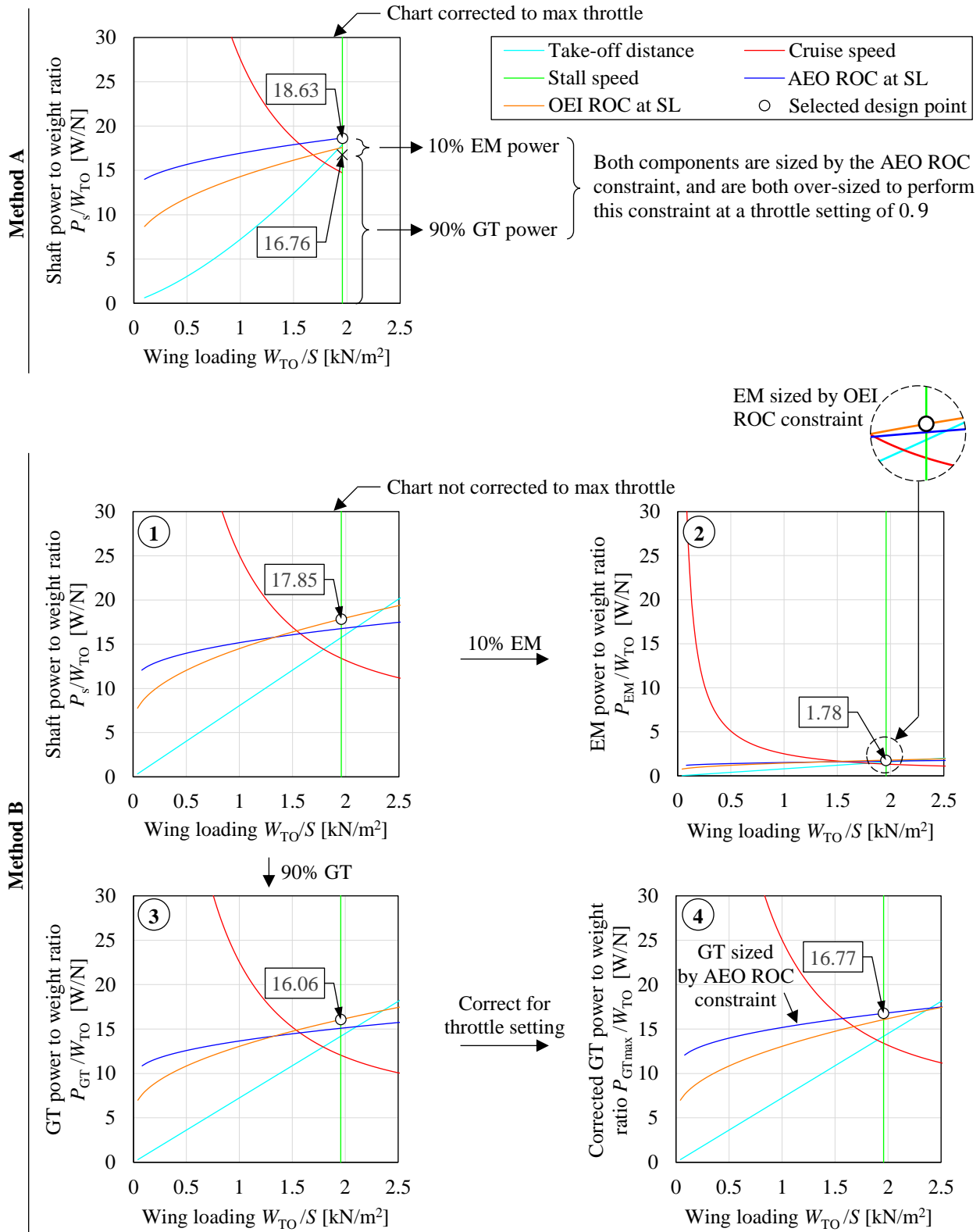


Fig. 11 Overview of how the constraint diagrams of Method A (top) and Method B (bottom) are used in the design process. Diagrams obtained for the parallel powertrain configuration.

the power-to-weight ratio required from the electric motors is much lower than the gas turbine, as visible in Figs. 11.B.2 and 11.B.3. Given that different throttle settings are used for different constraints (see Table A.2), the gas turbine has a different active constraint than the electric motors. Note that only the gas turbine is corrected for throttle setting, as shown in Fig. 11.B.4. Nevertheless, even though the two methods use fundamentally different approaches for the matching diagrams, the resulting design points are comparable. The gas-turbine power-to-weight ratio is virtually the same for both cases ($P_{GT}/W_{TO} = 16.76$ and 16.77 for methods A and B, respectively). The power-to-weight ratio obtained for the electrical motors is approximately 5% lower for Method B ($P_{EM}/W_{TO} = 1.87$ and 1.78 for methods A and B, respectively) since it is not throttle-corrected.

Using the P/W_{TO} and W_{TO}/S data from the constraint diagrams, the mission performance analysis is then carried out, and the aircraft's size is matched to the required mission performance. The resulting MTOM predicted by the two methods is presented in Table 8, including the difference of Method B with respect to Method A, which is calculated by $(MTOM_B - MTOM_A)/MTOM_A$. Additionally, the MTOM breakdown obtained for the short-range mission is shown in Fig. 12. In all cases, the differences between the two methods are well within the uncertainty of a Class-I sizing process. The most important conclusions that can be drawn are summarized in the following paragraphs.

Table 8 Maximum-take off mass values calculated for the conventional, parallel, serial, and fully-electric powertrain configurations using the two sizing methods. “N/A” indicates that no converged design was obtained.

Powertrain	Range [km]	Payload [t]	Method A	Method B	Difference [%]
			MTOM [t]	MTOM [t]	
Conventional	396	1.96	6.22	6.26	+0.7%
	1280	1.33	6.36	6.45	+1.3%
	2361	0.55	7.08	7.18	+1.4%
Parallel	396	1.96	6.36	6.39	+0.4%
	1280	1.33	7.06	7.10	+0.6%
	2361	0.55	13.47	13.36	-0.8%
Serial	396	1.96	8.30	8.25	-0.6%
	1280	1.33	12.52	12.35	-1.3%
	2361	0.55	N/A	N/A	N/A
Electric	396	1.96	8.17	8.29	+1.5%
	1280	1.33	N/A	N/A	N/A
	2361	0.55	N/A	N/A	N/A

1. Conventional Powertrain

The results for the conventional powertrain configuration (shown in Table 8) differ slightly from the results shown in Sec. III, due to the simplified modeling approach taken for the HEP comparison. The discrepancy is larger for the short- and long-range missions than for the medium-range mission. For both methods, the MTOM obtained for the short-range mission is lower than in Sec. III, because the average gas-turbine efficiency is accurate, but the fuel reserves are neglected. The MTOM obtained for the long-range mission, to the contrary, is over-predicted because, in this case, the exclusion of contingency fuel has a relatively lower impact, while the assumed gas-turbine efficiency is lower than in practice, due to the long cruise segment. Nevertheless, the agreement between both methods is good. The maximum difference in MTOM between method A and method B is less than 1.5%.

2. Parallel-Hybrid Powertrain

The results for the parallel hybrid powertrain (compare Fig. 4) show excellent agreement, with a difference of less than 1% between both methods. For both the parallel-hybrid and the serial-hybrid designs, the level of hybridization is fixed at 10%. For the parallel-hybrid, this means that the propeller is always supplied by 1 part electric motor power and 9 parts gas turbine power, joined through a gearbox with 100% efficiency. A converged design is obtained for all three missions, even though the long-range aircraft is more than twice as heavy as the short-range aircraft. Considering the very advanced technology assumptions that are made, this result indicates that efficient long-range flying with hybrid-electric propulsion systems is not a straightforward task. However, the detailed results for the short-range mission (Fig. 12) show that the fuel mass is reduced, when comparing against the conventional propulsion layout, even though MTOM increases.

3. Serial-Hybrid Powertrain

For this study, none of the prospective advantages (aero-propulsive interaction, distributed propulsion, etc.) of serial-hybrid designs are taken into account. The serial-hybrid powertrain is therefore expected to perform worse (heavier, less efficient) than the conventional or parallel-hybrid configurations. This is supported by the results presented in Table 8. Only the short- and medium-range mission have converged. For the long-range mission, the powertrain is too heavy and inefficient to converge—even with the highly optimistic technology assumptions. The results are very close (0.6% difference) for the short-range mission, and still provide an acceptable agreement (1.6% difference) for the medium-range mission. It is worth noting that, just as for the parallel-hybrid powertrain, the level of hybridization is fixed at 10%. This means that the electric motor is always supplied by 1 part battery power and 9 parts generator power.

4. Fully Electric Powertrain

The final analysis is conducted for the fully electric powertrain configuration. Even with the highly optimistic technology assumptions, only the short-range mission converges for this powertrain architecture, as shown in Table 8. The medium and long-range missions require an MTOM above 50 tons, which is infeasible for a 19-seat aircraft. Yet, both methods converged within 1.5% for the short-range mission. For this specific set of requirements and technology assumptions, the serial-hybrid short-range aircraft and the electric short-range aircraft converge to almost the same MTOM. In Fig. 12 it can be observed that the additional mass required by the batteries for the fully-electric configuration completely compensates the weight reduction due to the absence of gas turbines, fuel, and generators. However, while Method A predicts a higher MTOM than Method B for the serial-hybrid short-range case, it predicts a lower MTOM for the electric short-range case. Therefore, no clear conclusion can be drawn regarding which of the two methods is more (or less) conservative.

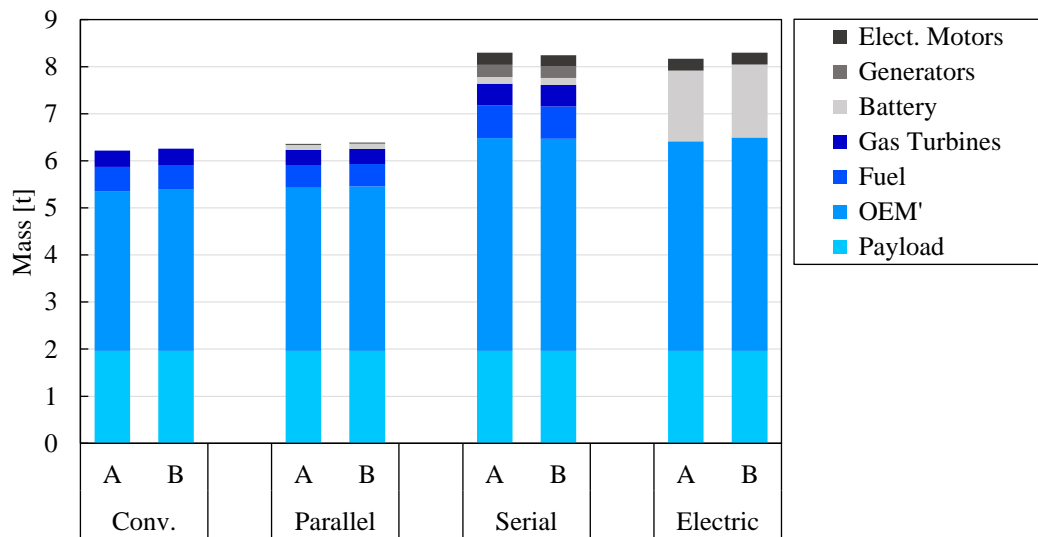


Fig. 12 Mass breakdown of the four powertrain configurations obtained using Method A and Method B, for the short-range mission ($R = 396$ km, $m_{PL} = 1.96$ t).

C. Parameter Sweeps

As a final step of this validation study, the design methods are evaluated regarding their ability to properly account for changes in the technology level and TLARs. The reader is reminded that the aim is to compare the data and gradients obtained with the two methods, and not to study the impact of these parameters on the resulting aircraft's design. In this process, the impact of three parameters is analyzed: range, battery specific energy, and the hybridization ratio. The baseline point for the parameter sweeps is the short-range mission. Thus, payload is fixed at 1.96 t, and the design range is fixed at 396 km. The baseline technology assumptions are the same as in Sec. IV.B, ($E_{bat}^* = 1500$ Wh/kg and $H_P = 0.1$). Mission range is swept between 100 km and 2500 km, battery specific energy is swept between 100 Wh/kg and 2000 Wh/kg, and the hybridization ratio is varied between 0 and 1, all while maintaining the remaining parameters constant.

The results for the parameter sweeps are analyzed for two measures of merit: MTOM and PREE. MTOM is often used for comparison in aircraft design studies since it gives an indication of the “size” of the aircraft and has a direct impact on power requirements, energy requirements, production and maintenance costs, and the certification of the aircraft [9]. The Payload-Range Energy Efficiency (PREE) [32], meanwhile, is used as the figure of merit to evaluate the energy consumption of the aircraft. The PREE is defined as payload weight times the range of the aircraft, divided by the total energy consumed during the nominal mission (excluding reserves), i.e.:

$$\text{PREE} = \frac{W_{\text{PL}} \cdot R}{E_{\text{miss}}} \quad (7)$$

Therefore, this dimensionless parameter indicates how efficiently the aircraft can transport its payload over a determined distance during its day-to-day operation. In Eq. 7, the energy consumed during the nominal mission, E_{miss} , is calculated differently by the two methods:

$$E_{\text{miss},A} = E_{\text{taxi out}} + E_{\text{TO}} + E_{\text{climb}} + E_{\text{cruise}} + E_{\text{descent}} \quad (8)$$

$$E_{\text{miss},B} = E_{\text{taxi out}} + E_{\text{TO}} + E_{\text{climb}} + E_{\text{cruise}} + E_{\text{descent}} + E_{\text{landing}} + E_{\text{taxi in}} \quad (9)$$

While Method B uses energy fractions that are known a priori for taxi, take-off, and landing (see Table A.5), Method A specifically calculates the energy consumption in these phases. The landing phase and the taxi-in phase are analyzed after flying the diversion. Thus, these phases would be analyzed at a wrong mass. To avoid confusion, these phases were entirely disregarded for the calculation of E_{miss} . Thus, E_{miss} will be slightly lower for Method A than for Method B, resulting in higher PREE values. Nevertheless, the difference was confirmed to be minor.

The following subsections detail the three parameter sweeps separately. Data for these comparisons are provided in the appendix so that these trade studies can be used as reference cases for benchmarking and validation of other design tools.

1. Range

The design range is varied from 100 km to 2500 km. Thus, short-range missions of just 15 min flight time are covered at the low end, while the longest flight would last 6 hours. Range is swept in steps of 100 km, and the results of the sweep are presented in Fig. 13.

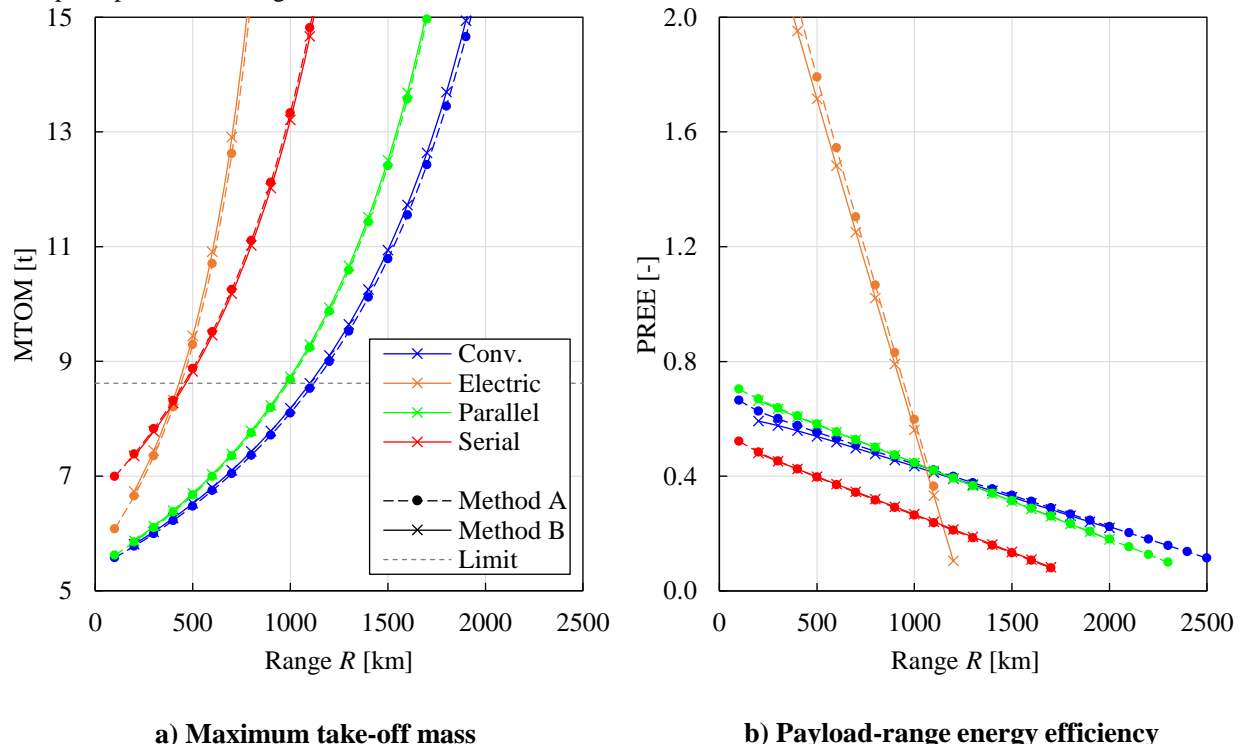


Fig. 13 Maximum take-off mass and PREE obtained for different mission ranges ($E_{\text{bat}}^* = 1500 \text{ Wh/kg}$, $H_P = 0.1$). The gray dashed line indicates the MTOM limit for a 19-passenger commuter aircraft per CS-23 regulations.

Both plots – MTOM, as well as PREE – correlate very well. All basic trends are captured. The MTOM plots show an exponential relationship for increasing ranges. The PREE plots drop almost linearly, as longer flights are analyzed. When analyzing MTOM results, the conventional aircraft shows to be less sensitive to an increase in range, when compared to the other designs. The serial and parallel designs show a similar slope but present an offset. This can be attributed to the mass increase, which is inherent to the hybrid propulsion systems. The fully electric design shows the highest slope. This behavior is expected, due to the much lower specific energy of batteries, compared to fossil fuels.

PREE shows an almost linear relationship with range. Again, the highest sensitivity is observed for the fully electric aircraft, and the lowest sensitivity is observed for the conventional design. This corresponds with the data of the MTOM analysis. When results for methods A and B are compared, they show only subtle differences for PREE. Method A always slightly overpredicts PREE. This is expected, because the energy summation is slightly different between the methods, as described previously. The difference is more pronounced at the lower ranges because the relative time spent for landing and taxi in is decreasing, as total flight time is increased. Therefore, the error is less relevant at long ranges.

If the CS-23 commuter mass limit of 8618 kg (19000 lb) would be enforced, then the maximum range of the fully electric and serial hybrid designs would be limited to less than 450 km, while the conventional aircraft could achieve ranges of 1100 km, more than twice as far. However, even though the conventional aircraft is the lightest, its PREE is inferior to the electric and parallel hybrid design at ranges up to 1100 km. This shows the general trend that electric and hybrid-electric aircraft can be more efficient for short-distance flights, while longer ranges are most likely to be carried out by conventional aircraft. However, these are unoptimized designs with extremely optimistic technology assumptions, and thus no quantitative conclusions should be drawn from this data.

2. Battery Technology Level

The specific energy E_{bat}^* of the batteries is varied from 100 Wh/kg to 2000 Wh/kg. At the same time, the specific power P_{bat}^* is varied to maintain a constant discharge rate of 4C. Thus, $P_{\text{bat}}^* = 0.4 \text{ kW/kg}$ at 100 Wh/kg, while $P_{\text{bat}}^* = 8 \text{ kW/kg}$ at 2000 Wh/kg. E_{bat}^* is varied in steps of 100 Wh/kg, and the results of the sweep are presented in Fig. 14. For the 4C discharge rate assumed, the battery mass was found to be sized by energy requirements in all cases, and not by power requirements. Thus, all missions are terminated with a 20% state-of-charge.

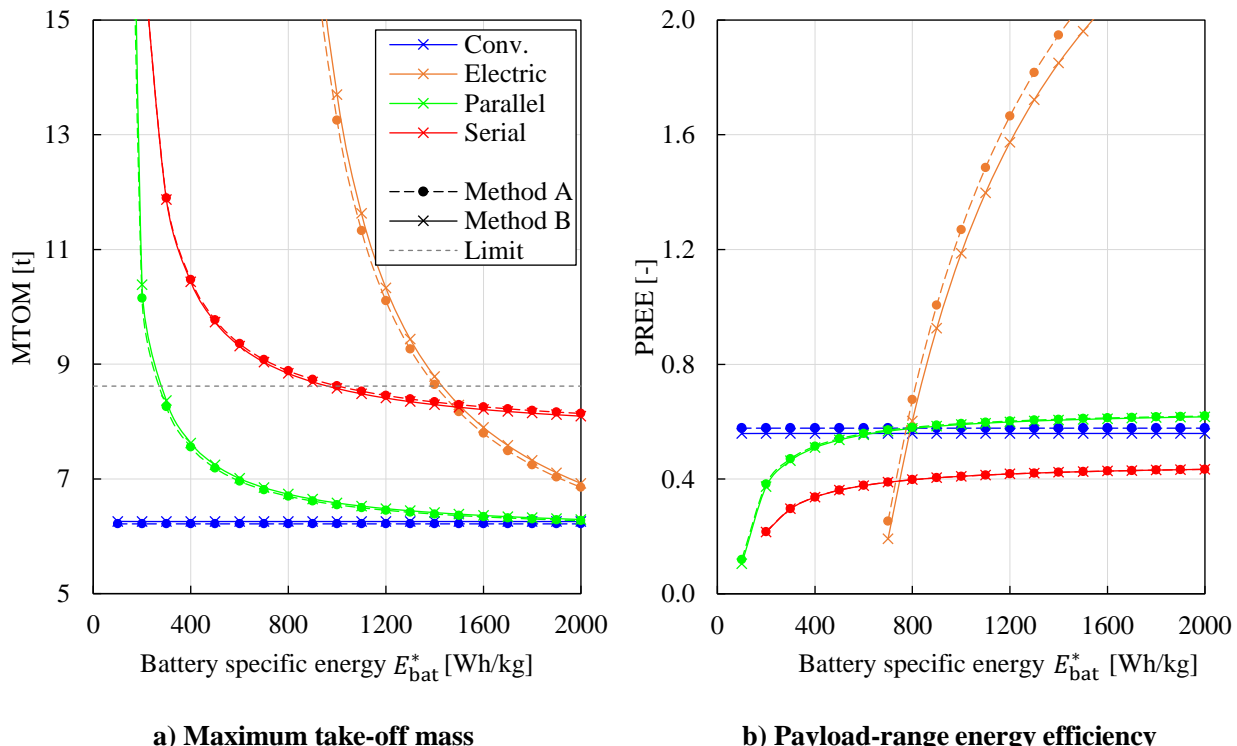


Fig. 14 Maximum take-off mass and PREE obtained for different battery technology levels ($R = 396 \text{ km}$, $H_P = 0.1$). The gray dashed line indicates the MTOM limit for a 19-passenger commuter aircraft per CS-23 regulations.

Again, the MTOM and PREE plots show very good correlation for all propulsion architectures. The expected trends are captured, with battery technology having no influence on conventional designs. For the remaining configurations, improving battery performance will yield lighter aircraft, which will be more efficient. Thus, for this study, PREE is roughly inversely proportional to MTOM. The absolute differences in MTOM between methods A and B are more pronounced at lower technology levels because the aircraft become heavier.

Method A again slightly over-predicts PREE, when compared to Method B. For this analysis, the relative error of the PREE calculation remains nearly constant across the sweep, because the mission is not varied. The difference in PREE is more evident for the fully electric configuration (approximately 5% for the baseline $E_{\text{bat}}^* = 1500 \text{ Wh/kg}$) and is also reflected in the MTOM comparison. This discrepancy is more prominent for the fully-electric configuration due to the higher battery weight fraction and subsequent higher sensitivity to battery specific energy.

Figure 13 shows that the CS-23 mass limit requires an E_{bat}^* of at least 1450 Wh/kg to allow for a fully-electric design. This indicates that electric propulsion systems will not be a drop-in replacement for conventional propulsion systems in the near future. However, a design with such kind of batteries would reach three times the PREE of the conventional aircraft. Benefits in terms of PREE can already be observed for batteries that exceed 800 Wh/kg. However, these aircraft would be four times heavier than comparable conventional aircraft, due to the snowball effect of the sizing process. Finally, Fig. 14 also shows that parallel architectures can present minor improvements in PREE if the battery specific energy is increased beyond 700 Wh/kg. Serial powertrains, on the other hand, are always outperformed by conventional fuel-based powertrains, since no hypothetical improvements in aero-propulsive efficiency or gas-turbine efficiency are included in this study.

3. Hybridization ratio

The hybridization ratio of the propulsion system is varied from 0% to 100% in steps of 10%. Note that the hybridization ratio is defined differently for serial and parallel powertrains, as discussed in Sec. II.C. In both cases, a hybridization ratio of 100 % corresponds to a fully electric aircraft, which exclusively uses batteries. However, for a serial architecture, a hybridization of 0% corresponds to a turboelectric aircraft, while for a parallel architecture, the powertrain is reduced to a conventional fuel-based engine. Consequently, Fig. 15 shows the results of the parameter sweeps for the serial and parallel powertrains, while the conventional and fully-electric configurations are obtained as limit cases of these two sweeps.

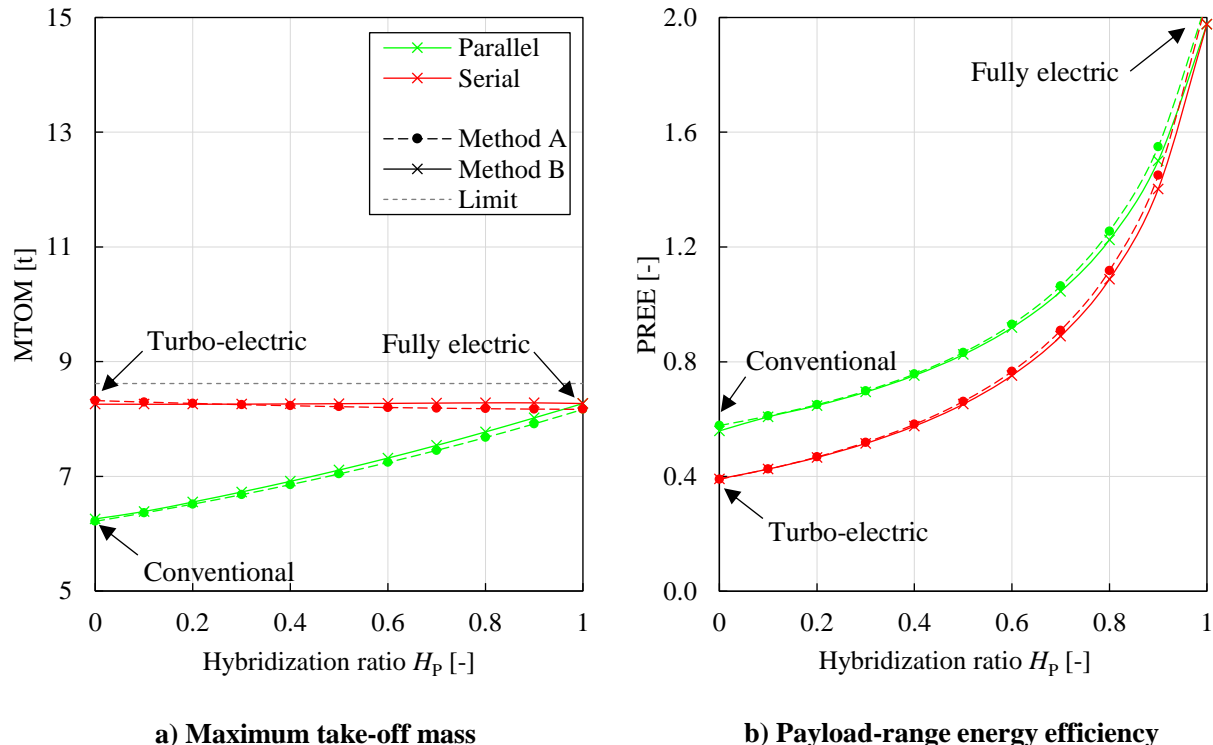


Fig. 15 Maximum take-off mass and PREE obtained for different hybridization ratios ($R = 396 \text{ km}$, $E_{\text{bat}}^* = 1500 \text{ Wh/kg}$). The gray dashed line indicates the MTOM limit for a 19-passenger commuter aircraft per CS-23 regulations.

Once more, the MTOM and PREE plots show a very good correlation between the methods for both propulsion architectures. The parallel hybrid with a hybridization ratio of 0 % corresponds to a conventional aircraft and is, therefore, the lightest solution for the given mission. As the hybridization ratio is increased, the relative size of the electric power systems of the aircraft increase. However, as MTOM increases, so does PREE. At 100% hybridization the fully electric configuration is reached. The data points, at $H_{P,PH} = 0.0, 0.1$, and 1.0 can also be found in the previous diagrams. The serial hybrid with a hybridization of 0 % corresponds to a turbo-electric propulsion configuration which uses no buffer battery. As $H_{P,SH}$ increases, the gas turbine size is reduced, and batteries are added, until the fully electric configuration is reached at $H_{P,SH} = 1.0$.

Figure 14a shows that MTOM is practically insensitive to the hybridization ratio, while PREE improves with increasing hybridization. The authors suspected that this almost constant relationship between H_P and MTOM is specific for this set of input parameters, and not a trend inherent to the type of propulsion system in general. To confirm this hypothesis, the hybridization sweep of the serial hybrid architecture was also conducted for batteries with a specific energy of 3000 Wh/kg. The results are not shown here, but for that case, MTOM was found to vary significantly with the level of hybridization. Therefore, the lack of a gradient is a coincidence. For the selected input parameters, the increase in battery mass as H_P increases compensates the decrease in engine, generator, and fuel mass.

V. Conclusions

In this study, two preliminary sizing methods for hybrid-electric aircraft are compared in detail. The two methods, developed at FH Aachen and TU Delft, respectively, are used to evaluate a 19-passenger commuter aircraft. The fuel-based reference aircraft is first sized for three points of the payload-range diagram. The results obtained from the two methods deviate from the reference data by approximately 1% in terms of power-to-weight ratio, and by less than 4% in terms of maximum take-off mass (MTOM). The discrepancy in MTOM is predominantly attributed to uncertainties in component modeling and variations in the mission profile.

The two methods are then used to evaluate parallel, serial, and fully-electric configurations. When comparing the different powertrain architectures for the three payload-range combinations selected, a difference in MTOM of less than 2% is observed between the two methods. Additionally, three parameter sweeps are performed, in order to analyze the sensitivity of MTOM and Payload-Range Energy Efficiency (PREE) to mission range, battery specific energy, and the hybridization ratio of the aircraft. The results of these sweeps show an excellent agreement in both slope and offset between the two methods. The largest deviations are observed for the fully-electric configuration, due to the sensitivity of the battery-weight fraction to energy consumption. This leads to a PREE difference between the two methods of approximately 5% for the baseline mission requirements and technology assumptions.

These differences observed lie well within the uncertainty of the Class-I sizing process and confirm the correct implementation of the two methods. Although this does not necessarily guarantee that the formulation of the methods is flawless—since both methods might coincidentally be based on the same, inaccurate assumption—the agreement of results significantly increases the confidence in these two formulations. This is further evidenced by the trends observed in the parameters sweeps, which coincide with those expected from literature. Moreover, throughout this study, the differences between the two methods are exposed as much as possible, such that the results can be used as a benchmark by the aircraft design community to compare and validate other design methods for hybrid-electric aircraft.

Acknowledgments

The authors would like to thank Maurice Hoogreef for helping with the evaluation of CS-23 requirements. The authors also thank Falk Götten, who provided valuable guidance on the set-up of the CFD simulation. Finally, the authors like to express their gratitude to Siemens PLM Software for providing academic licenses of their software StarCCM+.

References

- [1] Wilberforce, T., El-Hassan, Z., Khatib, F. N., Al Makky, A., Baroutaji, A., Carton, J. G., and Olabi, A. G., "Developments of Electric Cars and Fuel Cell Hydrogen Electric Cars," *International Journal of Hydrogen Energy*, pp. 25695-25734, 5 October 2017.
<https://doi.org/10.1016/j.ijhydene.2017.07.054>
- [2] De Breucker, S., Peeters, E., and Driesen, J., "Possible Applications of Plug-In Hybrid Electric Ships," in *2009 IEEE Electric Ship Technologies Symposium*, IEEE Publ., Piscataway, NJ, 2009, pp. 310–317.
<https://doi.org/10.1109/ESTS.2009.4906530>
- [3] Hepperle, M., "Electric Flight—Potential and Limitations," NATO MPAPVT-209-09, Energy Efficient Technologies and Concepts of Operation, Lisbon, Portugal, Oct. 2012.
- [4] Warwick, G., "Electric Potential - Are battery technologies advancing fast enough to enable eVTOL," *Aviation Week & Space Technology*, pp. 38-41, 14 August 2017.
- [5] Brelje, B. J., and Martins, J. R. R. A., "Electric, Hybrid, and Turboelectric Fixed-Wing Aircraft: A Review of Concepts, Models, and Design Approaches," *Progress in Aerospace Sciences*, Vol 104, pp. 1-19, 2018.
<https://doi.org/10.1016/j.paerosci.2018.06.004>
- [6] Moore, M. D., and Fredericks, B., "Misconceptions of Electric Propulsion Aircraft and their Emergent Aviation Markets," in *52nd Aerospace Sciences Meeting*, National Harbor, MD, USA, 2014.
<https://doi.org/10.2514/6.2014-0535>
- [7] Friedrich, C., and Robertson, P. A., "Hybrid-Electric Propulsion for Aircraft," *Journal of Aircraft*, pp. 176-189, February 2015.
<https://doi.org/10.2514/1.C032660>
- [8] Raymer, D. P., *Aircraft Design: A Conceptual Approach*, 6th ed., Reston, VA, USA: AIAA, 2018.
- [9] Nicolai, L. M. and Carichner, G. E., *Fundamentals of Aircraft and Airship Design - Volume I - Aircraft Design*, Reston, VA, USA: AIAA, 2010.
- [10] Gudmundsson, S., *General Aviation Aircraft Design: Applied Methods and Procedures*, Oxford, Great Britain: Butterworth-Heinemann, 2014.
- [11] Mattingly, J. D., Heiser, W. H., and Pratt, D. T., *Aircraft Engine Design*, 2nd ed., Reston, VA, USA: AIAA, 2002.
- [12] Roskam, J., *Airplane Design Part I-VIII*, Wichita, KS, USA : Roskam Aviation and Engineering Corp., 1985.
- [13] Loftin, L. K., Jr., Subsonic Aircraft: Evolution and the Matching of Size to Performance, NASA-RP-1060, Langley, VA, USA: NASA Langley, 1980.
<https://ntrs.nasa.gov/search.jsp?R=19800020744>.
- [14] Herzog, J., Artist, *Dornier Do 228NG at ILA Berlin Air Show 2012*. [Art]. Wikipedia, 2012.
- [15] Juretzko, P. G., Immer, M. and Wildi, J., "Performance analysis of a hybrid-electric retrofit of a RUAG Dornier Do 228NG," *CEAS Aeronautical Journal*, 26 Sep 2019.
<https://doi.org/10.1007/s13272-019-00420-2>
- [16] Hofmann, J., Stumpf, E., Weintraub, D., Köhler, J., Pham, D., Schneider, M., Dickhoff, J., Burkhart, B., Reiner, G., Spiller, M. and Werner, E. A., "A Comprehensive Approach to the Assessment of a Hybrid Electric Powertrain for Commuter Aircraft," in *AIAA Aviation Forum 2019*, Dallas, TX, USA, 2019.
<https://doi.org/10.2514/6.2019-3678>
- [17] RUAG Aerospace Services GmbH, "Dornier 228 Advanced Commuter (AC) Facts & Figures," Wessling, Germany, 2015.
- [18] Dornier GmbH, Logistic, Pilot's Operating Handbook Including the LBA Approved Airplane Flight Manual - Dornier 228-100, Munich, Germany: Dornier GmbH, 1983.
- [19] Honeywell, "TPE331-10 Turboprop Engine Brochure," Honeywell Aerospace, Phoenix, TX, USA, 2016.
- [20] IHS Markit, "RUAG (Dornier) 228 NG," Jane's All the World's Aircraft: Development & Production, 23 January 2019. [Online]. Available: <https://janes.ihs.com/JAWADevelopmentProduction/Display/jawa704-jawa>. [Accessed 7 November 2019].
- [21] Finger, D. F., Braun, C., and Bil, C., "Initial Sizing Methodology for Hybrid-Electric General Aviation Aircraft," *Journal of Aircraft*, 2019.
<https://doi.org/10.2514/1.C035428>
- [22] Finger, D. F., Braun, C., and Bil, C., "Case Studies in Initial Sizing for Hybrid-Electric General Aviation Aircraft," in *AIAA/IEEE Electric Aircraft Technologies Symposium (EATS)*, Cincinnati, IN, USA, 2018.
<https://doi.org/10.2514/6.2018-5005>

- [23] Rings, R., Ludowicy, J., Finger, D. F., and Braun, C., "Sizing Studies of Light Aircraft with Parallel Hybrid Propulsion Systems," in *67. Deutscher Luft- und Raumfahrtkongress DLRK 2018*, Friedrichshafen, Germany, 2018. <https://doi.org/10.25967/480227>
- [24] Ludowicy, J., Rings, R., Finger, D. F., and Braun, C., "Sizing Studies of Light Aircraft with Serial Hybrid Propulsion Systems," in *67. Deutscher Luft- und Raumfahrtkongress DLRK 2018*, Friedrichshafen, Germany, 2018. <https://doi.org/10.25967/480226>
- [25] Finger, D. F., Götten, F., Braun, C., and Bil, C., "Mass, Primary Energy, and Cost – The Impact of Optimization Objectives on the Initial Sizing of Hybrid-Electric General Aviation Aircraft," in *68. Deutscher Luft- und Raumfahrtkongress DLRK 2019*, Darmstadt, Germany, 2019. <https://doi.org/10.25967/490012>
- [26] Finger, D. F., Braun, C., and Bil, C., "Comparative Assessment of Parallel-Hybrid-Electric Propulsion Systems for Four Different Aircraft," in *2020 AIAA Aerospace Sciences Meeting*, Orlando, FL, USA, 2020.
- [27] Finger, D. F., Braun, C., and Bil, C., "Initial Sizing for a Family of Hybrid-Electric VTOL General Aviation Aircraft," in *67. Deutscher Luft- und Raumfahrtkongress DLRK 2018*, Friedrichshafen, Germany, 2018. <https://doi.org/10.25967/480102>
- [28] de Vries, R., Brown, M. T. H., and Vos, R., "Preliminary Sizing Method for Hybrid-Electric Distributed-Propulsion Aircraft," *Journal of Aircraft*, Vol. 56, Issue 6, 2019. <https://doi.org/10.2514/1.C035388>
- [29] Hoogreef, M. F. M., Vos, R., de Vries, R., and Veldhuis, L. L. M., "Conceptual Assessment of Hybrid Electric Aircraft with Distributed Propulsion and Boosted Turbofans," in *2019 AIAA Aerospace Sciences Meeting*, San Diego, CA, USA, 2019. <https://doi.org/10.2514/6.2019-1807>
- [30] Hoogreef, M. F. M., de Vries, R., Sinnige, T., and Vos, R., "Synthesis of Aero-Propulsive Interaction Studies applied to Conceptual Hybrid-Electric Aircraft Design," in *2020 AIAA Aerospace Sciences Meeting*, Orlando, FL, USA, 2020.
- [31] Orefice, F., Della Vecchia, P., Ciliberti, D., and Nicolosi, F., "Aircraft Conceptual Design Including Powertrain System Architecture and Distributed Propulsion," in *AIAA Propulsion and Energy 2019 Forum*, Indianapolis, IN, USA, 2019. <https://doi.org/10.2514/6.2019-4465>
- [32] de Vries, R., Hoogreef, M. F. M., and, Vos, R., "Preliminary Sizing of a Hybrid-Electric Passenger Aircraft Featuring Over-the-Wing Distributed-Propulsion," in *2019 AIAA Aerospace Sciences Meeting*, San Diego, CA, USA, 2019. <https://doi.org/10.2514/6.2019-1811>
- [33] de Vries, R., Hoogreef, M. F. M., and Vos, R., "Aeropropulsive Efficiency Requirements for Turboelectric Transport Aircraft," in *2020 AIAA Aerospace Sciences Meeting*, Orlando, FL, USA, 2020.
- [34] de Vries, R., Brown, M. T. H., and Vos, R., "A Preliminary Sizing Method for Hybrid-Electric Aircraft Including Aero-Propulsive Interaction Effects," in *2018 Aviation Technology, Integration, and Operations Conference*, Atlanta, GA, USA, 2018. <https://doi.org/10.2514/6.2018-4228>
- [35] Finger, D. F., Braun, C., and Bil, C., "An Initial Sizing Methodology for Hybrid-Electric Light Aircraft," in *2018 Aviation Technology, Integration, and Operations Conference*, Atlanta, GA, USA, 2018. <https://doi.org/10.2514/6.2018-4229>
- [36] Torenbeek, E., *Synthesis of Subsonic Airplane Design*, Delft, The Netherlands: Delft University Press, 1982.
- [37] National Academies of Sciences, Engineering, and Medicine, Commercial Aircraft Propulsion and Energy Systems Research: Reducing Global Carbon Emissions, Washington, D.C., USA: National Academies Press, 2016.
- [38] Finger, D. F., Götten, F., Braun, C., and Bil, C., "On Aircraft Design Under the Consideration of Hybrid-Electric Propulsion Systems," in *The Proceedings of the 2018 Asia-Pacific International Symposium on Aerospace Technology (APISAT 2018)*, Singapore, Springer, 2019, pp. 1261-1272.
- [39] Stoll, A. M., and Mikic, G. V., "Design Studies of Thin-Haul Commuter Aircraft with Distributed Electric Propulsion," in *16th AIAA Aviation Technology, Integration, and Operations Conference*, Washington, D.C., USA, 2016. <https://doi.org/10.2514/6.2016-3765>
- [40] Finger, D. F., Braun, C., and Bil, C., "A Review of Configuration Design for Distributed Propulsion Transitioning VTOL Aircraft," in *Asia-Pacific International Symposium on Aerospace Technology - APISAT2017*, Seoul, Korea, 2017.
- [41] Ko, A., Schetz, J. A., and Mason, W. H., "Assessment of the Potential Advantages of Distributed-Propulsion for Aircraft," in *XVI International Symposium on Air Breathing Engines (ISABE)*, Cleveland, OH, USA, 2003.
- [42] Jackson, P., Jane's All the World's Aircraft: Development & Production 2017-2018, Coulsdon, Great Britain: IHS Markit, 2017.
- [43] International Civil Aviation Organization, Annex 6, Operation of Aircraft, Part I: International Commercial Air Transport — Aeroplanes, Montreal, Canada: International Civil Aviation Organization, 2016.

- [44] Hoerner, S. F., *Fluid-Dynamic Drag*, Bricktown, NJ, USA: Hoerner Fluid Dynamics, 1965.
- [45] Götten, F., Havermann, M., Braun, C., Gómez, F., and Bil, C., "On the Applicability of Empirical Drag Estimation Methods for Unmanned Air Vehicle Design," in *2018 Aviation Technology, Integration, and Operations Conference*, Atlanta, GA, USA, 2018.
<https://doi.org/10.2514/6.2018-3192>
- [46] Götten, F., Finger, D. F., Havermann, M., Marino, M., and Bil, C., "A Review of Guidelines and Best Practices for Subsonic Aerodynamic Simulations using RANS CFD," in *Asia-Pacific International Symposium on Aerospace Technology - APSIAT 2019*, Gold Coast, Australia, 2019.
- [47] Hirsch, C., *Computational Methods for Inviscid and Viscous Flows*, Chichester, Great Britain: Wiley, 2002.
- [48] Schlichting, H., and Gersten, K., *Boundary-Layer Theory*, 9th ed., Berlin, Germany: Springer, 2017.
- [49] Obert, E., *Aerodynamic Design of Transport Aircraft*, Amsterdam, The Netherlands: IOS Press, 2009.
- [50] European Aviation Safety Agency, "Acceptable Means of Compliance and Guidance Material to Certification Specifications for Normal-Category Aeroplanes (CS-23)," European Aviation Safety Agency, Cologne, Germany, 2017.
- [51] ASTM F3179/F3179M-16, "Standard Specification for Performance of Aeroplanes," ASTM International, West Conshohocken, PA, USA, 2016.
- [52] Jansen, R. H., Bowman, C., Jankovsky, A., Dyson, R., and Felder, J., "Overview of NASA Electrified Aircraft Propulsion Research for Large Subsonic Transports," in *53rd AIAA/SAE/ASEE Joint Propulsion Conference*, Atlanta, GA, USA, 2017.
<https://doi.org/10.2514/6.2017-4701>

Appendix

Table A.1 Additional design parameters and assumptions which are not included in Tables 2, 4, and 7.

Parameter	Value	Parameter	Value
Number of propellers [-]	2	Take-off lift coefficient $C_{L,TO}$ [-] ^a	1.34
PMAD efficiency η_{PM} [-]	1.0	$\Delta C_{L,max}$, take-off flaps [-]	0.73
Gearbox efficiency η_{GB} [-]	1.0	$\Delta C_{L,max}$, landing flaps [-]	0.97
Fuel specific energy E_f^* [MJ/kg] ^{1,b}	42.8	$\Delta C_{D,min}$, take-off flaps [-] ^b	0.010
Empty weight fraction OEM/MTOM [-] ^b	0.600	$\Delta C_{D,min}$, landing flaps [-] ^b	0.045
Empty weight fraction OEM'/MTOM [-] ^a	0.545	$\Delta C_{D,min}$, landing gear [-] ^b	0.015
Ambient density [kg/m ³]	ISA	$\Delta C_{L,min,D}$, take-off flaps [-] ^b	0
Ambient temperature [°C]	ISA	$\Delta C_{L,min,D}$, landing flaps [-] ^b	0
Coefficient of rolling friction [-] ^a	0.04	Δe , take-off flaps [-] ^b	0.040
Maximum lift coefficient (clean) $C_{L,max}[-]$	1.70	Δe , landing flaps [-] ^b	0.125

^a Parameters only required for Method A

^b Parameters only required for Method B

¹ Note that BSFC = $1/(\eta_{GT} E_f^*)$

Table A.2 Assumed aircraft properties per performance constraint and mission segment. A dash (-) indicates that the quantity is not an input, but a computed value.

	Throttle [-]	Velocity [m/s]	Mass fraction m/m_{TO} [-]	Propulsive efficiency [-]	Flap setting	Landing gear position
Constraints	Cruise	0.9	115	1	0.8	retracted
	Take-off	1	- ^a / $1.2V_s^{b,1}$	1	0.7	take-off
	Landing	0.9	34.6	1	0.8	landing
	AEO ROC	0.9	$V_{best\ climb}^{a,1} / 1.2V_s^{b,1}$	1	0.7	retracted
	OEI ROC	1	$V_{best\ climb}^{a,1} / 1.2V_s^{b,1}$	1	0.65	retracted
Mission analysis	Climb	0.9	-	-	0.8	retracted
	Cruise	-	115	-	0.8	retracted
	Descent	0,10 ^a / 0,05 ^b	-	-	0.8	retracted
	Div. Climb	0.9	-	-	0.8	retracted
	Div. Cruise	-	82	-	0.8	retracted
	Div. Descent	0,10 ^a / 0,05 ^b	-	-	0.8	retracted
	Loiter	-	$53^a / V_{max\ endurance}^b$	-	0.8	retracted

^a Values used for Method A

^b Values used for Method B

¹ Stall speed in the flight condition considered

Table A.3 Component masses and wing area obtained in the reference aircraft comparison.

Mission	Method	MTOM [kg]	OEM [kg]	m_{PL} [kg]	m_f [kg]	m_{GT} [kg]	S [m^2]
396 km	Reference	6400	3900	1960	540	349	32.0
	A	6641	3866	1960	615	356	32.3
	B	6416	3865	1960	591	354	32.2
1280 km	Reference	6400	3900	1325	1175	349	32.0
	A	6434	3862	1325	1247	356	32.2
	B	6403	3857	1325	1221	353	32.1
2361 km	Reference	6400	3900	547	1953	349	32.0
	A	6489	3895	547	2047	359	32.5
	B	6188	3728	547	1914	341	31.0

Table A.4 Component masses and wing area obtained for the four different powertrain configurations in the HEP comparison study. “N/A” indicates no converged design was obtained.

Config.	Mission	Method	MTOM [kg]	OEM [kg]	m_{PL} [kg]	m_f [kg]	m_{bat} [kg]	m_{GT} [kg]	m_{GEN} [kg]	m_{EM} [kg]	S [m^2]
Conv.	396 km	A	6216	3731	1960	525	0	343	0	0.0	31.1
		B	6259	3770	1960	529	0	345	0	0.0	31.4
	1280 km	A	6364	3820	1325	1219	0	352	0	0.0	31.9
		B	6446	3883	1325	1238	0	356	0	0.0	32.3
	2361 km	A	7083	4252	547	2285	0	391	0	0.0	35.5
		B	7182	4325	547	2310	0	396	0	0.0	36.0
Parallel	396 km	A	6361	3803	1960	486	113	316	0	19.7	31.9
		B	6385	3830	1960	481	115	317	0	18.9	32.0
	1280 km	A	7058	4219	1325	1222	292	351	0	21.8	35.4
		B	7102	4259	1325	1222	296	352	0	21.0	35.6
	2361 km	A	13472	8054	547	3924	947	670	0	41.6	67.5
		B	13363	8014	547	3863	939	663	0	39.5	66.9
Serial	396 km	A	8295	5490	1960	697	148	457	256	256	41.6
		B	8246	5452	1960	686	148	453	243	244	41.3
	1280 km	A	12518	8284	1325	2389	519	690	386	387	62.7
		B	12354	8168	1325	2348	513	679	364	365	61.9
	2361 km	A	N/A	N/A	N/A	N/A	N/A	N/A	N/A	N/A	N/A
		B	N/A	N/A	N/A	N/A	N/A	N/A	N/A	N/A	N/A
Electric	396 km	A	8168	4704	1960	0	1504	0	0	252	40.9
		B	8294	4784	1960	0	1550	0	0	245	41.6
	1280 km	A	N/A	N/A	N/A	N/A	N/A	N/A	N/A	N/A	N/A
		B	N/A	N/A	N/A	N/A	N/A	N/A	N/A	N/A	N/A
	2361 km	A	N/A	N/A	N/A	N/A	N/A	N/A	N/A	N/A	N/A
		B	N/A	N/A	N/A	N/A	N/A	N/A	N/A	N/A	N/A

Table A.5 Taxi, take-off, and landing energy fractions assumed for Method B, based on the estimations of Method A, for the three missions considered. Energy fractions expressed as a percentage of total installed energy (including reserves). “N/A” indicates no converged design was obtained.

		Short range $R = 396 \text{ km}$, $m_{PL} = 1960 \text{ kg}$	Medium range $R = 1280 \text{ km}$, $m_{PL} = 1325 \text{ kg}$	Long range $R = 2361 \text{ km}$, $m_{PL} = 547 \text{ kg}$
Conventional	Taxi out & take-off	2.6%	1.3%	0.8%
	Landing & taxi in	1.6%	0.8%	0.5%
Parallel	Taxi out & take-off	2.1%	0.9%	0.6%
	Landing & taxi in	0.7%	0.3%	0.2%
Serial	Taxi out & take-off	2.2%	0.9%	N/A
	Landing & taxi in	0.7%	0.3%	N/A
Electric	Taxi out & take-off	1.6%	N/A	N/A
	Landing & taxi in	0.1%	N/A	N/A

Table A.6 Hybridization-ratio sweep results obtained from methods A and B ($m_{PL} = 1960 \text{ kg}$, $R = 396 \text{ km}$, $E_{bat}^* = 1500 \text{ Wh/kg}$).

H_p [-]	Parallel				Serial			
	MTOM [kg]		PREE [-]		MTOM [kg]		PREE [-]	
	A	B	A	B	A	B	A	B
0.0	6216	6258	0.577	0.559	8321	8258	0.390	0.392
0.1	6361	6386	0.611	0.608	8295	8256	0.426	0.426
0.2	6515	6552	0.650	0.647	8271	8257	0.468	0.466
0.3	6679	6727	0.698	0.694	8250	8259	0.519	0.515
0.4	6855	6912	0.757	0.752	8231	8262	0.582	0.575
0.5	7042	7109	0.832	0.825	8214	8266	0.661	0.652
0.6	7241	7318	0.930	0.919	8200	8272	0.766	0.752
0.7	7452	7540	1.064	1.045	8188	8277	0.909	0.889
0.8	7676	7774	1.255	1.225	8179	8281	1.118	1.087
0.9	7914	8019	1.549	1.500	8172	8281	1.449	1.402
1.0	8168	8269	2.060	1.976	8168	8269	2.060	1.976

Table A.7 Range sweep results obtained from methods A and B ($m_{PL} = 1960$ kg, $E_{bat}^* = 1500$ Wh/kg, $H_p = 0.1$). “N/A” indicates no converged design was obtained.

Range [km]	Conventional						Parallel						Serial					
	MTOM [kg]		PREE [-]		MTOM [kg]		PREE [-]		MTOM [kg]		PREE [-]		MTOM [kg]		PREE [-]		MTOM [kg]	
	A	B	A	B	A	B	A	B	A	B	A	B	A	B	A	B	A	B
100	5576	N/A	0.665	N/A	5619	N/A	0.703	N/A	6991	N/A	0.522	N/A	6080	N/A	2.281	N/A		
200	5777	5812	0.627	0.592	5850	5871	0.669	0.664	7384	0.484	0.480	0.480	6654	6733	2.666	2.461		
300	5993	6030	0.600	0.577	6100	6122	0.638	0.634	7823	0.453	0.452	0.452	7349	7445	2.329	2.197		
400	6225	6267	0.576	0.558	6372	6397	0.610	0.607	8316	0.426	0.425	0.425	8206	8327	2.049	1.952		
500	6476	6521	0.553	0.539	6669	6696	0.582	0.580	8875	0.397	0.398	0.398	9289	9443	1.792	1.715		
600	6747	6798	0.531	0.518	6994	7025	0.555	0.553	9513	0.370	0.372	0.372	10701	10907	1.545	1.482		
700	7041	7098	0.509	0.498	7353	7386	0.528	0.526	10249	0.344	0.346	0.346	12620	12905	1.303	1.251		
800	7362	7426	0.487	0.477	7749	7786	0.501	0.499	11106	0.317	0.320	0.320	15377	15801	1.066	1.020		
900	7713	7785	0.465	0.456	8190	8231	0.474	0.473	12119	0.291	0.293	0.293	19675	20372	0.831	0.790		
1000	8099	8179	0.443	0.434	8683	8730	0.447	0.446	13333	0.264	0.267	0.267	27309	28669	0.597	0.561		
1100	8524	8615	0.421	0.413	9239	9293	0.421	0.419	14816	0.238	0.241	0.241	44623	48357	0.365	0.333		
1200	8996	9100	0.399	0.392	9870	9931	0.394	0.393	16668	0.212	0.214	0.214	N/A	N/A	N/A	N/A		
1300	9523	9641	0.377	0.370	10594	10663	0.367	0.366	19045	0.185	0.188	0.188	N/A	N/A	N/A	N/A		
1400	10115	10250	0.355	0.349	11430	11511	0.341	0.339	22209	0.159	0.162	0.162	N/A	N/A	N/A	N/A		
1500	10785	10939	0.334	0.327	12408	12505	0.314	0.313	26627	0.133	0.135	0.135	N/A	N/A	N/A	N/A		
1600	11548	11726	0.312	0.305	13569	13684	0.287	0.286	33234	0.106	0.109	0.109	N/A	N/A	N/A	N/A		
1700	12428	12634	0.290	0.284	14968	15106	0.261	0.259	44187	0.080	0.083	0.083	N/A	N/A	N/A	N/A		
1800	13451	13691	0.268	0.262	16686	16857	0.234	0.232	N/A	N/A	N/A	N/A	N/A	N/A	N/A	N/A		
1900	14657	14940	0.246	0.241	18848	19064	0.207	0.206	N/A	N/A	N/A	N/A	N/A	N/A	N/A	N/A		
2000	16099	16407	0.224	0.220	21651	21932	0.180	0.179	N/A	N/A	N/A	N/A	N/A	N/A	N/A	N/A		
2100	17854	18270	0.202	0.197	25431	25808	0.154	0.152	N/A	N/A	N/A	N/A	N/A	N/A	N/A	N/A		
2200	20039	20558	0.180	0.175	30804	31356	0.127	0.125	N/A	N/A	N/A	N/A	N/A	N/A	N/A	N/A		
2300	22830	23491	0.158	0.154	39050	39912	0.100	0.098	N/A	N/A	N/A	N/A	N/A	N/A	N/A	N/A		
2400	26522	27405	0.136	0.132	N/A	54876	N/A	0.072	N/A	N/A	N/A	N/A	N/A	N/A	N/A	N/A		
2500	31637	32871	0.114	0.110	N/A	87721	N/A	0.045	N/A	N/A	N/A	N/A	N/A	N/A	N/A	N/A		

Table A.8 Battery specific-energy sweep results obtained from methods A and B ($m_{PL} = 1960$ kg, $R = 396$ km, $H_p = 0.1$). “N/A” indicates no converged design was obtained.

E_{bat}^* [Wh/ kg]	Conventional						Parallel						Serial						Electric							
	MTOM [kg]		PREE [-]		MTOM [kg]		PREE [-]		MTOM [kg]		PREE [-]		MTOM [kg]		PREE [-]		MTOM [kg]		PREE [-]		MTOM [kg]		PREE [-]			
	A	B	A	B	A	B	A	B	A	B	A	B	A	B	A	B	A	B	A	B	A	B	A	B		
100	6216	6259	0.577	0.559	32546	37160	0.119	0.104	N/A	N/A	N/A	N/A														
200	6216	6257	0.577	0.559	10153	10385	0.383	0.374	16321	16352	0.216	0.215	N/A	N/A	N/A	N/A	N/A	N/A	N/A	N/A	N/A	N/A	N/A	N/A		
300	6216	6257	0.577	0.559	8259	8365	0.470	0.464	11895	11868	0.297	0.296	N/A	N/A	N/A	N/A	N/A	N/A	N/A	N/A	N/A	N/A	N/A	N/A		
400	6216	6257	0.577	0.559	7555	7626	0.514	0.509	10474	10437	0.337	0.337	N/A	N/A	N/A	N/A	N/A	N/A	N/A	N/A	N/A	N/A	N/A	N/A		
500	6216	6257	0.577	0.559	7187	7243	0.541	0.536	9774	9733	0.361	0.361	N/A	N/A	N/A	N/A	N/A	N/A	N/A	N/A	N/A	N/A	N/A	N/A		
600	6216	6257	0.577	0.559	6961	7007	0.558	0.554	9357	9314	0.377	0.377	N/A	N/A	N/A	N/A	N/A	N/A	N/A	N/A	N/A	N/A	N/A	N/A		
700	6216	6257	0.577	0.559	6808	6848	0.571	0.567	9080	9036	0.389	0.389	66422	85005	0.253	0.253	0.191	0.191	0.191	0.191	0.191	0.191	0.191	0.191	0.191	
800	6216	6257	0.577	0.559	6697	6734	0.580	0.576	8883	8838	0.398	0.398	0.397	0.397	24862	26951	0.677	0.677	0.603	0.603	0.603	0.603	0.603	0.603	0.603	0.603
900	6216	6257	0.577	0.559	6614	6647	0.587	0.584	8736	8690	0.404	0.404	0.404	0.404	16724	17551	1.006	1.006	0.925	0.925	0.925	0.925	0.925	0.925	0.925	0.925
1000	6216	6257	0.577	0.559	6549	6580	0.593	0.590	8621	8576	0.410	0.410	0.410	0.410	13253	13698	1.270	1.270	1.186	1.186	1.186	1.186	1.186	1.186	1.186	1.186
1100	6216	6257	0.577	0.559	6496	6526	0.598	0.595	8530	8484	0.414	0.414	0.414	0.414	11329	11628	1.485	1.485	1.398	1.398	1.398	1.398	1.398	1.398	1.398	1.398
1200	6216	6257	0.577	0.559	6453	6481	0.602	0.599	8455	8409	0.418	0.418	0.418	0.418	10107	10329	1.665	1.665	1.573	1.573	1.573	1.573	1.573	1.573	1.573	1.573
1300	6216	6257	0.577	0.559	6417	6444	0.605	0.602	8393	8347	0.421	0.421	0.421	0.421	9261	9436	1.817	1.817	1.722	1.722	1.722	1.722	1.722	1.722	1.722	1.722
1400	6216	6257	0.577	0.559	6387	6413	0.608	0.605	8340	8294	0.423	0.423	0.423	0.423	8642	8784	1.947	1.947	1.850	1.850	1.850	1.850	1.850	1.850	1.850	1.850
1500	6216	6257	0.577	0.559	6361	6386	0.611	0.608	8295	8249	0.426	0.426	0.426	0.426	8168	8289	2.060	2.060	1.960	1.960	1.960	1.960	1.960	1.960	1.960	1.960
1600	6216	6257	0.577	0.559	6338	6362	0.613	0.610	8256	8209	0.428	0.428	0.428	0.428	7794	7899	2.159	2.159	2.057	2.057	2.057	2.057	2.057	2.057	2.057	2.057
1700	6216	6257	0.577	0.559	6318	6341	0.615	0.612	8222	8175	0.430	0.430	0.430	0.430	7492	7584	2.246	2.246	2.143	2.143	2.143	2.143	2.143	2.143	2.143	2.143
1800	6216	6257	0.577	0.559	6300	6323	0.617	0.614	8192	8145	0.431	0.431	0.431	0.431	7242	7324	2.323	2.323	2.218	2.218	2.218	2.218	2.218	2.218	2.218	2.218
1900	6216	6257	0.577	0.559	6285	6307	0.618	0.616	8165	8118	0.433	0.433	0.433	0.433	7032	7107	2.393	2.393	2.286	2.286	2.286	2.286	2.286	2.286	2.286	2.286
2000	6216	6257	0.577	0.559	6271	6292	0.620	0.617	8141	8094	0.434	0.434	0.434	0.434	6853	6922	2.455	2.455	2.348	2.348	2.348	2.348	2.348	2.348	2.348	2.348